UiT
THE ARCTIC
UNIVERSITY
OF NORWAY

Faculty of Science and Technology

Department of Physics and Technology

Chip Based Optical Nanoscopy: System Integration and Automation

—

Daniel Henry Hansen

Fys-3900 Master's thesis in Physics - May 2019

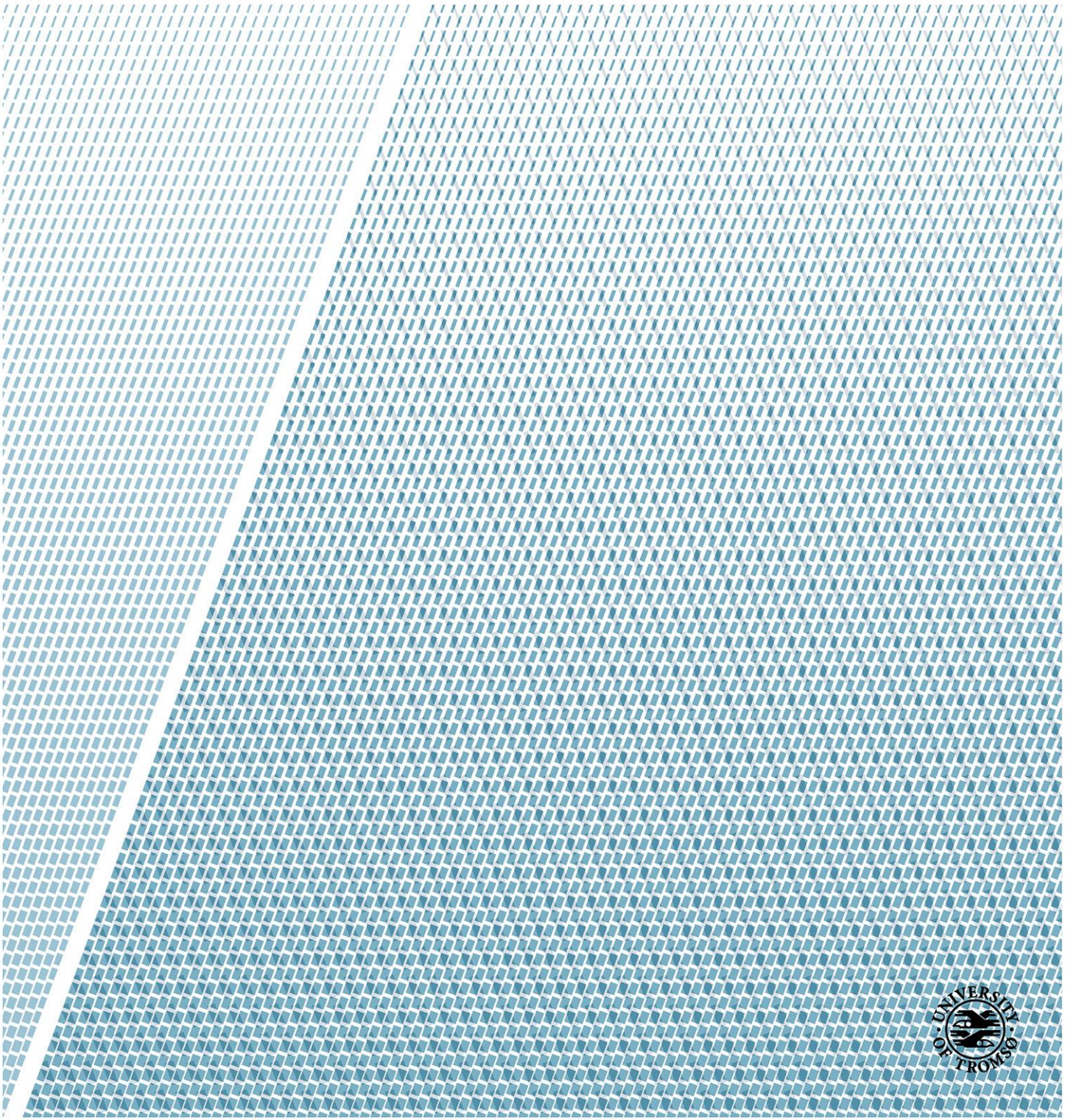

Abstract

An integrated photonic chip based nanoscopy system has previously been developed at UiT, which allows for several advantages over conventional total internal reflection fluorescence microscopy and nanoscopy (i.e. super-resolution nanoscopy). While the proof-of-concept has been demonstrated, there were several important system optimization tasks that were needed for making the system practical and more usable.

This thesis tackles three major system optimization tasks, namely efficient and automatic coupling of light into waveguide in the photonic chip, precise control and stabilization of feed point into the waveguide, and synchronization of illumination and collection arms of the photonic chip based microscope. Electronic and optomechanical instrumentation, along with optimization algorithms and work flow design, are used to accomplish these tasks.

The specific accomplishments of the thesis are described next. For a novel and more flexible light feed setup designed at the department, a new mechanism for measuring the coupling efficiency was designed, an initial coupling and parasitic inter-axis cross-talk compensation mechanism was designed, and two optimization algorithms were explored for the final fine coupling. Testing of the implementation showed promising results with close to optimal coupling efficiency achieved in a reasonable amount of time. A piezoelectric stage with large travel range was tuned to provide the best possible performance in terms of speed and accuracy for precise control and stabilization of the feed point across the width of the waveguide. This was used to adapt a nanoscopy algorithm named multiple signal classification algorithm (MUSICAL) for exploiting the variable illumination property of multimode waveguides on the photonic chip. Lastly, the system synchronization was achieved so that the shift and stabilization of the feed point, the trigger of camera read time, and the writing of data into the computer memory can work in tandem with each other with almost no fallow time and no compromise on the image acquisition quality even if hundreds to thousands of images have to acquired continuously in a single measurement. Thus, the goals of this thesis were achieved successfully and the practical use of the photonic-chip for microscopy and nanoscopy was greatly enhanced.

Dedication

I would like to take the opportunity to thank my supervisors, Jean-Claude, Krishna and Balpreet. Jean-Claude and Krishna in particular have provided help and support beyond what could reasonably be expected. So, thank you.

Contents

List of Figures **ix**

List of Tables **xi**

List of Listings **xiii**

List of Abbreviations **xv**

1 Introduction **1**

1.1 Motivation 1

1.2 Outline 2

2 Background **5**

2.1 Chip-Based Microscopy 5

2.1.1 Waveguide Principle 5

2.1.2 Planar Waveguides 7

2.1.3 Total Internal Reflection for Fluorescence Microscopy . . 8

2.1.4 Waveguides for Microscopy 8

2.1.5 Multimode Waveguides and Super-Resolution 11

2.2 Current Chip-Based Microscopy Setup 12

2.3 Multiple Signal Classification Algorithm (MUSICAL) 13

2.3.1 Principle 13

2.3.2 MUSICAL-on-Chip 13

3 System Integration and Automation **15**

3.1 Optimization of Illumination Set-Up of Current Chip-Based Microscope 15

3.1.1 Photodiode Amplifier and Computer Interface 17

3.1.2 Power Supply for TIA and ADC 18

3.1.3 Transimpedance Amplifier 18

3.1.4 Analog to Digital Converter 18

3.1.5 Arduino and Firmware for Computer Interface 18

3.2 Initial Alignment 19

3.2.1 Edge Finding Method 19

3.2.2 Implementation 21
3.2.3 Stage Cross-talk Correction 22
3.2.4 Conclusion about initial alignment 23
3.3 Automated Optimization of Coupling Efficiency 24
3.3.1 Measuring the Coupling Efficiency 25
3.3.2 Process Concept 25
3.3.3 Method 1: Gradient Descent 26
3.3.4 Method 2: Nelder-Mead Simplex Algorithm 28
3.3.5 Performance Simulation - Without Noise 28
3.3.6 Performance Simulation - Including Noise 29
3.3.7 Conclusion and Implementation 32
3.4 Controlled Multimode Illumination 33
3.4.1 Motivation 33
3.4.2 Methodology 34
3.4.3 Mode of Operation 34
3.4.4 Tuning the Control System 35
3.4.5 Sensor Noise 37
3.4.6 Settling Time 38
3.4.7 Conclusion 40
3.5 PI Stage and Camera Synchronization 40
3.5.1 Motivation 40
3.5.2 Methodology 41
3.5.3 Software Performance 42
3.5.4 Multimode Control 42
3.5.5 MUSICAL-on-chip 43
3.5.6 Conclusion 45

4 Discussion and Outlook **47**
4.1 Summary of the accomplished work 47
4.2 Impact of the Accomplished Work 48
4.3 Future Outlook 49

List of Figures

1 Visualization of the variables in Snell's when light refracts through different media [9]. 5

2 Refracted (top) vs. totally internal reflected light yielding evanescent waves (bottom) [11]. 6

3 Simulation of an MMI coupler, showing a multimode interference pattern stemming from the interference and difference in propagation constants of modes [13]. 7

4 a. Different planar waveguide geometries, with typical materials and dimensions as used for imaging at the UiT group. b. Example of chip with arrows showing multiple straight waveguides for imaging purposes [4]. 8

5 a) EPI vs. TIRF illumination mechanism at the microscope objective [15]. b) Scheme of typical commercial TIRF setup [16]. 9

6 Fluorescence signal of waveguides with a homogeneously stained surface. Left: geometry designed for single-mode propagation (25 μm wide). Right: highly multimode waveguide showing interference pattern (50 μm wide). 10

7 Scheme of chip-based microscopy setup. 12

8 When coupling into wide multimode waveguides, different locations of feed point result in different illumination patterns. 14

9 Alternative setup consisting of one translation stage with custom-designed aluminum mount, including motorized actuators (1) for the sample stage (5), integrated coupling section (2-4), and measurement system for automatic coupling adjustment (6-7). 15

10 Scheme of photodiode assembly and types of light reaching each, generating the signal for the automatic coupling process. The axes definition represented here will be followed for the rest of this thesis. 16

11 Schematic of setup developed to read the signal of photodiode pair. Top circuit shows a linear 3.3 V voltage regulator providing filtered power to the op-amps and ADC. Bottom circuit, from left to right: transimpendance amplifiers are connected to an ADC converter, which is connected to an Arduino. 17

12 Left: Gaussian profile of the beam in the propagation direction. In black, obstruction symbolizing the waveguide edge placed in the beam path. Right: Intensity profile of the coupling beam at the focal spot (y=0). 19

13 Simulation of stray light signal vs. chip edge position. (a) Gaussian beam profile (blue) with translated path of obstruction for y- (red) and z-axes (black). (b) Stray light signal for obstruction scanned over y-axis. (c) Stray light signal for obstruction scanned over z-axis. 20

14 Experimental profiles of stray light signal scanned over (a) y-axis, (b) z-axis and (c) repeated for the y-axis, with indicated waists and thresholds. The asymmetry compared the ideal model from Fig. 14 and position refinement in (c) after optimizing the orthogonal axis in (b) are visible. 22

15 Translation of stage over x axis and its influence on y (top) and z (bottom) axes, measured through stray light signal. The non flat trajectory displays a crosstalk between the axes. 22

16 Linear least squares-based polynomial fit of stage crosstalk for y- (top left) and z-axes (top right) when translating the x-axis, including residual values for the fit (bottom plots). 24

17 (a) Metal piece ("fence") attached to chip holder allowing for repeatable placement of chip in the y-axis. (b) Scheme of side view showing the fence's placement so that it does not interfere with the coupling beam. 24

18 Left: coupled light signal measured as function of coupling objective's relative position. The sectioned lines go through the maximum for each axis. Right: plot of sectioned lines marked in the left graph, clearly showing the asymmetry between the axis. . 26

19 Block diagram illustrating the Nelder-Mead simplex algorithm. . 29

20 Using the measured coupling efficiency from Fig. 18, simulations show the path taken for 10 different starting positions at 100 iterations (black) for the gradient descent algorithm (a) and Nelder-Mead simplex algorithm (b), including the evolution of the function value for both (c, d). 30

21 Contour of region of measured data selected for simulations including noise. 30

22 Performance of optimization algorithms on simulated dataset, 0-1% added noise. Black circles show the starting points, red circles the end points. 31

23 Performance of optimization algorithms on simulated dataset, 5-10% added noise. Black circles show the starting points, red circles the end points. 32

24 Labview interface of implemented automated coupling optimization. 33

25 Stick-slip drive mechanism [42]. 35

26 Control algorithm for the PI Q-522.140 stage [43]. 36

27 Open loop step response in frequency domain of PI stage, showing a resonant peak at 170 Hz. 37

28 Position control of stage was turned off to determine the sensor noise. 38

29 (a) Position error of PI stage for different step sizes over time. Error signal has been smoothed with a sliding average filter with a width of 20 samples. (b) Settling time as function of the square root of step size, with fit demonstrating linear proportionality between the axes. 38

30 Step response of PI stage shows direction dependent asymmetry. 39

31 Averaged step response of Fig. 30 to determine stage settling time shows oscillatory response which is stronger in the positive direction. 40

32 UI-handler of the synchronization software. 41

33 user interface of synchronization software. 42

34 (a) Timing diagram of the three software tasks during stage-camera synchronization, settling and exposure time being 20 ms. (b)-(d): Histograms of each task. From (b) it seems the stage task takes less than 20 ms in many cases. As the settling is implemented as a fixed delay after initiating movement of the stage, this is not possible and indicates an underestimation of the time spent here. (c) shows the camera task requiring approximately 15 ms longer than the exposure time. (d) shows that the time spent writing files is usually longer than that of the stage task, lowering performance of the system. 43

35 Illumination patterns created by scanning coupling feed point along input facet of waveguide. Waveguide width: 200 µm, 60x 1.2 NA objective, 100 nm step acquisition, 561 nm excitation, autofluorescence signal. (a) Single frame of the stack, with visible interference patterns. Green and yellow lines indicate the pixels used to create (c) and (d), respectively. (b) Mean image of the stack, demonstrating complete illumination of waveguide surface. In (c) and (d), one axis corresponds to the line from (a) scanned over the stack, respective axes indicated in each image. This illustrates the light modulation over each axis. 44

36 Fibroblast cells from mice imaged for actin on the chip setup. A stack of 281 images with 100 nm step size of the illumination spot was taken from a 320 µm wide, 150 nm tall Si_3N_4 strip waveguide. (a) Single frame of stack, showing multimode interference. (b) Mean image, removing multimode interference. (c) MUSICAL rendering of data. (d) Comparison between mean and MUSICAL images, with indicated line profile plotted in (e). The large improvement in resolution through the MUSICAL algorithm is visible at the dense signal region. 46

List of Tables

1 Approximations to crosstalk compensation functions 23

2 Results from simulations shown in Fig. 22 and 23. 31

3 Effect of increasing Proportional, integral and derivative gains K_p, K_i and K_d 36

4 Control loop parameters for the PI-stage controller, comparing factory default settings and settings found to produce a stable system response. 37

Listings

1 Pseuodocode representation of edge finding method 21
2 Pseuodocode representation of modified gradient descent algorithm. 27

Abbreviations

ADC Analog to digital converter

dSTORM direct Stochastic Optical Reconstruction Microscopy

RMSE Root mean square error

ESI Entropy-based Super-resolution Imaging

Fig. Figure

HIC High refractive index contrast

IIC Inter-integrated circuit

LMPFLFLN Long Working Distance M Plan Semi-Apochromat

MMI Multimode interference

MUSICAL Multiple Signal Classification Algorithm

NA Numerical aperture

PDMS Polydimethylsiloxane

PID Proportional-integral-derivative

PoI Point of interest

PSF Point spread function

sCMOS scientific complementary metal–oxide–semiconductor

SMC Single mode condition

SOFI Super-resolution Optical Fluctuation Imaging

SRRF Super-Resolution Radial Fluctuations

TIA Transimpedance amplifier

TIR Total internal reflection

TIRF Total internal reflection flourescence

UI User interface

UiT UiT - The Arctic University of Norway

USB Universal Serial Bus

1 Introduction

The invention of the optical microscope led to many new discoveries in the field of biology and medicine. However, there has always been a limit to the resolution available to researchers utilizing them. In the first period after the invention, increasing the resolution could be achieved by advances in the quality of optical components and by developing the understanding of the image forming process. By the end of the 19^{th} century, the understanding of light and the laws governing its propagation had advanced to a point where a fundamental limit to the achievable resolution in an optical system could be discerned. The mathematical formulation of this limit, attributed to Ernst Abbe, considers the achievable resolution in a microscope as a function of the numerical aperture (NA) of the objective lens [1, 2]. This physical limit will always be present for the researcher employing optical microscopes.

Methods that can circumvent this barrier have emerged within the last 20 years [3]. Widely referred to as "optical nanoscopy" or super-resolution microscopy, these techniques are typically fluorescence-based and employ different photo-chemical phenomena suitable for different applications to achieve super-resolution. They also often require complex bulk optics set-up for engineering the illumination, which is considered critical in achieving super-resolution.

The established optical nanoscopy approaches use complex microscopes but typically standard sample preparation on a glass slide. On the other hand, the Nanoscopy Group at the University of Tromsø develops integrated photonic chips which substitute glass slides as the sample substrate [4]. Inherent properties of the chip-based approach offer novel possibilities to nanoscopy methods in compact footprint. This is mainly because waveguides in the photonic chip can support creation of complex sample illumination needed for super-resolution and their delivery to the sample resting on its surface without using other bulk optical components for illumination engineering [5]. Thereby, the photonic chip can be retrofitted into a regular microscope to convert it into a nanoscope.

1.1 Motivation

Chip-based nanoscopy has been demonstrated by the group at UiT [4, 5, 6, 7], but it sill lacks user-friendly and efficient ways to control the setup. One of the aspects which requires proper implementation is the coupling of light into the waveguides in the photonic chip. As the chips are used as substrates, they are constantly exchanged. With each exchange, the initial coupling and its optimization has to undertaken afresh. This has been a manual process so far. Even with training and experience, an experienced user still requires a certain amount of time to complete the process, which can lead to bleaching and photodamage of the specimen even before imaging it. Moreover, different regions of interest may lie on different waveguides, which demands translation of the chip and realignment of the coupling. An automatized coupling mechanism was therefore of high interest, cutting down light exposure which can be detrimental for the specimen and helping widespread the technology through user-friendliness by eliminating alignment procedures.

As the photonic chip platform is being adapted for different nanoscopy methods, different illumination and image acquisition mechanisms have to be developed, which in turn calls for coordination and control of various components of the set-up. For instance, the fluctuation based nanoscopy approach named multiple signal classification algorithm (MUSICAL for brevity) [8], the expertise of which is available in-house at UiT, requires synchronization between the light feed point into the waveguide and the imaging camera. As several hundreds of frames, one for each feed point, are needed for this method, an automatized process here is absolutely necessary.

This thesis shows the development of the aforementioned points: automated initial alignment, automated coupling optimization and the setup synchronization for MUSICAL. The implementations reach beyond the mechanical and software-based solutions. Developing them allows for a better understanding of the setup's possibilities and limitations, provides new insights into the physical fundamentals of the applied methods and aids thus to their scientific and commercial progress.

1.2 Outline

This thesis is divided in four chapters. This first chapter presents an introduction to the field and the motivation of this work. The 2$^{\text{nd}}$ chapter provides a background for the understanding of chip-based microscopy. It encompasses the theory basics and discusses the differences and relevance compared to conventional microscopy, the setup components, and the work in the field so far. The end of the chapter discusses MUSICAL and the advantages of implementing it in the photonic-chip platform.

The 3$^{\text{rd}}$ chapter presents the novel contributions of this thesis. This chapter is divided into 5 sections:

1. A new setup configuration with additional control elements is introduced, providing a more practical and compact structure and implementing the detection method utilized in upcoming sections.

2. A method is developed which can adequately place the desired waveguide for initial coupling, correcting for imperfections of the translation stage.

3. Two algorithms for the automated optimization of coupling efficiency are implemented and compared on their performance using a computer model based on measured dependency of coupling efficiency on alignment of waveguide and excitation beam. Based on results acquired from the model, one is selected and implemented on the setup.

4. A stage for controlled illumination towards the realization MUSICAL-on-chip is tuned and characterized.

5. An interface is developed which synchronizes the stage from the previous section to the imaging system, enabling MUSICAL-on-chip. Measurement characteristics and a first result of MUSICAL-on-chip are presented.

The last chapter summarizes and concludes the accomplished work, providing an outlook on future possibilities.

2 Background

This chapter presents the background of the thesis. It includes the technological background, underlying technical concepts, and the general context of the present thesis. It is divided into three sections, namely chip-based microscopy, the current chip-based microscopy set-up that served as the starting point of this thesis, and Multiple Signal Classification Algorithm (MUSICAL) that motivates the need of the work undertaken in this thesis.

2.1 Chip-Based Microscopy

2.1.1 Waveguide Principle

A waveguide is, as the name implies, a device that confines a wave. Most often, this term is applied to devices intended to guide electromagnetic waves. as this thesis is concerned, we are interested in confining visible light. To understand how such devices work, it can be beneficial to start with a model using ray optics. Snells law [9] states that:

$$n_1 sin\theta_1 = n_2 sin\theta_2, \tag{1}$$

where n_1 and n_2 are the refractive indices of the media in Fig. 1, and θ_1 and θ_2 are the angles of the incident and refracted rays respectively, as represented in Fig. 1.

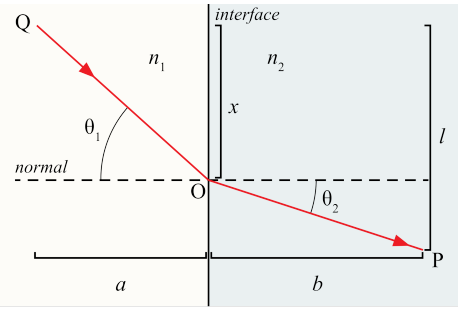

Figure 1: Visualization of the variables in Snell's when light refracts through different media [9].

Solving for θ_2 we obtain:

$$\theta_2 = arcsin\Big(\frac{n_1}{n_2} sin\theta_1\Big). \tag{2}$$

Considering the case where $n_1 > n_2$ it is clear that there is a critical angle $\theta_1 = \theta_c$ where $\frac{n_1}{n_2} sin\theta_c = 1$. It is then apparent that for $\theta_c < \theta_1 < \pi - \theta_c$ that θ_2 is a complex number. The framework of ray optics does not provide a clear interpretation of this. It turns out that this is because no light is refracted in this case, and the phenomenon of total internal reflection (TIR) occurs.

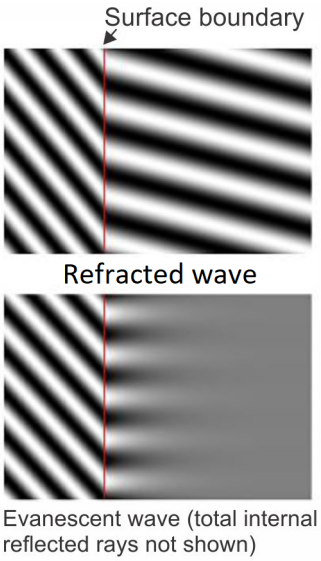

Figure 2: Refracted (top) vs. totally internal reflected light yielding evanescent waves (bottom) [11].

A more accurate model of the problem may be formed using an electromagnetic model of light. It can then be found that the reflection of light at a boundary between two dielectric materials depends on its polarization, as well as angle of incidence and material properties. It is assumed that the materials are homogeneous, linear, isotropic and absent of free charges and currents. The phenomenon can then be modeled using the Fresnel equations [10]. We can then find the portions of light reflected and refracted as functions of angle of incidence, and indeed the phenomenon of total internal reflection occurs. Due to the absence of free charges in the material, there cannot be a discontinuity in the field components parallel to the boundary. The consequence of this is that there must be a field penetrating into the medium of lower reflective index even though it does not propagate. This is known as the evanescent field, and it decays exponentially away from the boundary. Fig. 2 illustrates refraction vs. total internal reflection and the formation of evanescent waves.

Knowing the conditions for total internal reflection (TIR), one can imagine a continuous repetition of the phenomenon by having opposed surface boundaries fulfilling the TIR condition. In this case, interference between reflected waves will occur, achieving a constructive propagation after the self-consistency principle [12] if the total phase accumulated in one cycle is a multiple of 2π. Such a situation leads to a discrete set of modes supported in this waveguide, being a function of its dimensions, materials and the wavelength [12]. The propagating modes will have different propagation constants, that is the group velocity of modes are different. This means that as a set of modes are excited in the waveguide, the intensity seen will be an interference of the modes, and this distribution will change along the propagation length of the waveguide, as shown in Fig. 3.

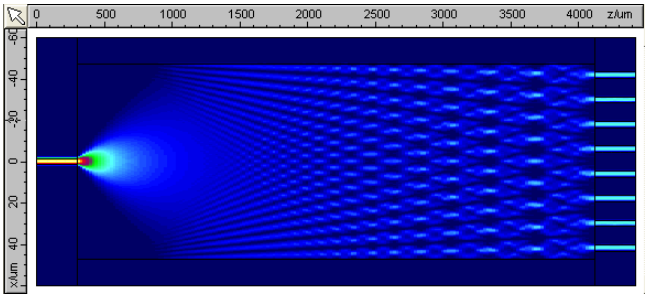

Figure 3: Simulation of an MMI coupler, showing a multimode interference pattern stemming from the interference and difference in propagation constants of modes [13].

2.1.2 Planar Waveguides

Planar waveguides can be one dimensional, confining the light only in the top and bottom (slab waveguides). Or. they may present laterally defined structures which confine light in two dimensions (rib or strip waveguides, also known under other names) [14]. A scheme of the different geometries is displayed in Fig. 4a, with a mention of materials and dimensions used at the UiT for imaging applications which will be discussed later in this chapter.

The different geometries exhibit their own advantages, being best suitable for different applications. Here, we discuss the strip and rib waveguides comparatively for the benefit of the readers. Whereas a certain amount of the laterally undefined slab is still present rib waveguides, this is completely removed at the strip configuration. In either geometry, propagation losses are always present as the etched sidewalls are never perfectly flat. Since strip geometries have larger exposed sidewall areas, they exhibit higher propagation losses than the rib geometry. On the other hand, strip waveguides have lower losses through bent sections because the mode confinement in rib geometries is lower because of the possibility of light guiding into the slab layer. However, in rib geometries it is easier to limit the number of propagating modes down to the single mode condition, which can be difficult to achieve in strip geometries as it would demand very narrow widths for the same material height and wavelength.

Planar waveguides and integrated optical systems in general are typically fabricated with technology from the semiconductor industry, whose well developed infrastructure allows for mass production at low cost. Generally, a silicon wafer is used as a substrate. As silicon has a high refractive index and it is not transparent under visible wavelengths, often a silicon dioxide layer is grown or deposited on the surface to serve as substrate for the waveguide. The guiding layer may then be deposited on top, before photoresist is applied and exposed using an appropriate mask, with the desired shape of the waveguide subsequently produced by etching. Fig. 4b shows such a chip from the UiT's Nanoscopy group, with arrows pointing towards the input of several straight waveguides on a single chip.

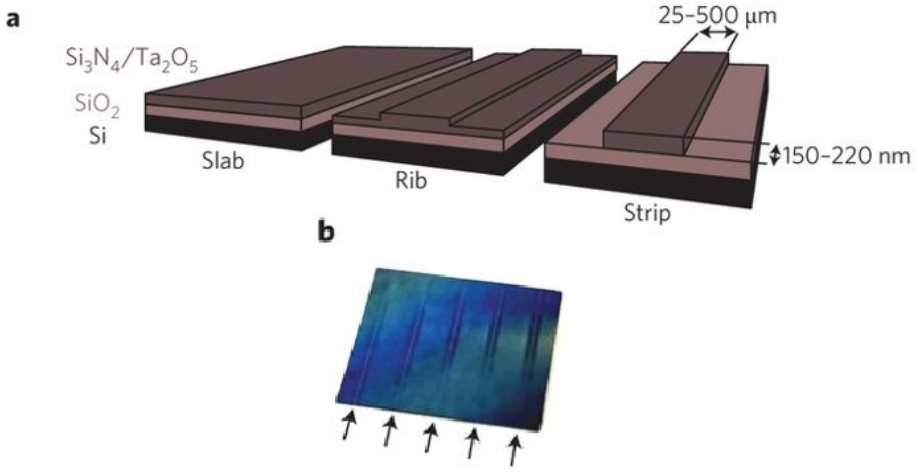

Figure 4: a. Different planar waveguide geometries, with typical materials and dimensions as used for imaging at the UiT group. b. Example of chip with arrows showing multiple straight waveguides for imaging purposes [4].

2.1.3 Total Internal Reflection for Fluorescence Microscopy

In fluorescence microscopy, the most common type of illumination ("epi") focuses the excitation laser in the center of the back focal plane of the imaging objective, achieving a collimated beam at the image plane (Fig. 5a, left side) [15]. If the focused beam is moved to the corner of the back aperture of a high numerical aperture (NA) objective, TIR can be achieved at the sample plane (Fig. 5a, right side) [15]. A sample imaged in epifluorescent illumination results into a different image than TIRF (total internal reflection fluorescence), since TIRF only excites a few hundreds of nanometers into the sample through the exponential decaying evanescent field [16], therefore achieving a thin optical section. This limited optical section results into removal of out-of-focus signal from the image, and thereby providing good contrast and a high signal to noise ratio. Some typical drawbacks of this way of performing TIRF are, e.g., the small field of view given by the high NA necessary to achieve TIR, the necessary readjustment of the beam placement at the back focal plane when changing the excitation wavelength, and the high price of the typically dedicated objectives together with the complicated excitation light path (Fig. 5 b).

2.1.4 Waveguides for Microscopy

The evanescent field of planar waveguides can also be utilised to excite fluorescent samples, while making use of a microscope to collect the fluorescence signal. By removing the excitation light path from the microscope, the complexity and dimensions of the setup can be significantly reduced. As waveguides can be designed to be several hundreds of micrometers wide, TIRF excitation over an almost arbitrarily wide field-of-view can be achieved while being independent of the collection optics.

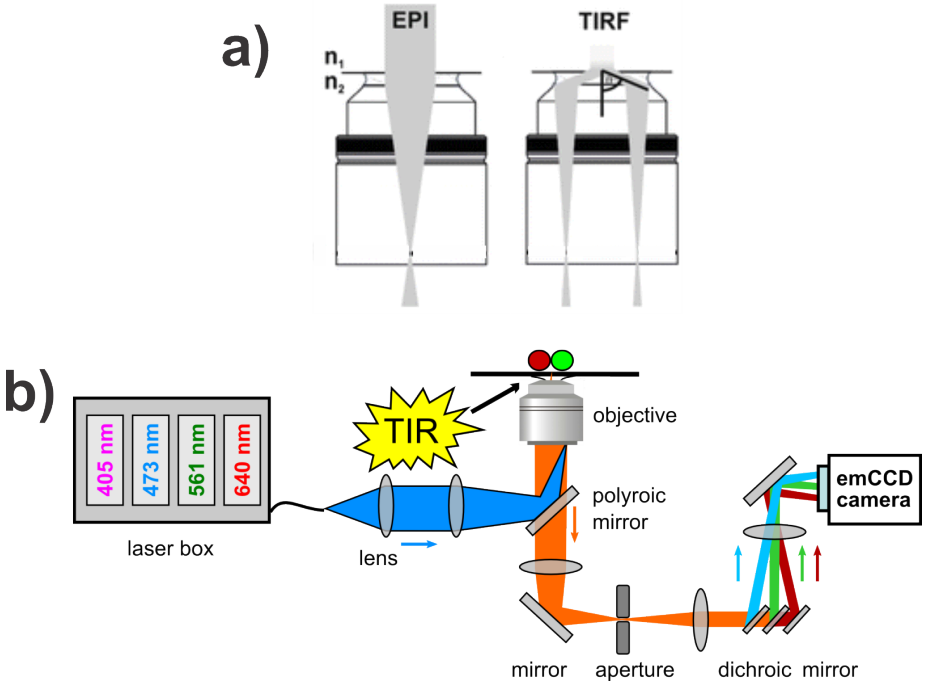

Figure 5: a) EPI vs. TIRF illumination mechanism at the microscope objective [15]. b) Scheme of typical commercial TIRF setup [16].

First manuscripts following this concept made use of slab waveguides to image fixed or live cells using fluorescent dyes [17, 18, 19, 20, 21] or, more recently, through a label-free approach [22]. A strong development to this field has been contributed by the group at the UiT. Beyond demonstration of homogenous, multicolor illumination for live cell imaging on waveguide chips [5] , the group in Tromsø was also the first to demonstrate waveguide-based imaging beyond the diffraction limit [23, 4, 7]. At UiT, photonic-chip platform is being adapted for using different super-resolution techniques such as single-molecule localization (dSTORM) [24], structured illumination microscopy (SIM) [25] or fluctuation methods (MUSICAL [8], ESI [26], SRRF [27], SOFI [28]).

Key to such developments are the utilized materials, waveguide geometries, and mechanisms of coordination between inducing different waveguide modes and acquiring images of the sample. By making use of high-refractive index contrast (HIC) materials such as Si_3N_4 (silicon nitride) or Ta_2O_5 (tantalum pentoxide) for the guiding layer (refractive index of ~ 2 at visible wavelengths) and SiO_2 (silicon dioxide) for substrate and cladding (refractive index of ~ 1.46), tight mode confinement is achieved. This in turn allows miniaturization of the structures and reduction of the structural footprints. Working with thin layers of guiding material, e.g., 150 nm, further leads to a considerable fraction of the mode to be available as evanescent field, typically reaching $\sim$ 200 nm into a sample deposited on the surface.

For many cases, a homogeneous illumination over the waveguide surface is desirable. This can be achieved when only guiding a zero order, fundamental mode through the waveguide. For the 150 nm HIC waveguides, a very shallow rib etch is necessary to fullfill the single-mode condition (SMC). A narrow width supports a deeper rib height, so that a width of 1.5 µm is chosen. This width is on the lower limit for which conventional photolithography can still provide reproducible results. Simulations using these dimensions suggest that a rib height of ca. 4 nm is needed to fulfill the SMC down to the typical bioimaging wavelength of 488 nm [6, 5]. As a width of 1.5 µm is not useful for imaging, adiabatic tapering has been used here to expand the initial width to 25 µm while maintaining the SMC [5, 7].

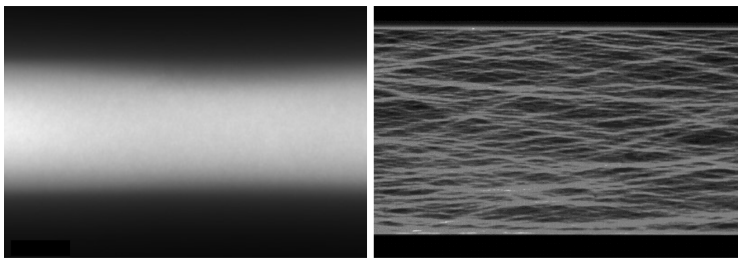

Figure 6: Fluorescence signal of waveguides with a homogeneously stained surface. Left: geometry designed for single-mode propagation (25 µm wide). Right: highly multimode waveguide showing interference pattern (50 µm wide).

However, experiments have shown that the calculated dimensions might not completely provide single-mode waveguides down to 488 nm, possibly due to parameter variations during fabrication. It was also demonstrated how curved

sections can eliminate interfering higher-order modes through their higher bend losses. It is evident that the single-mode condition for the given guiding layer height is demanding in terms of fabrication. Deeper etch depths or larger widths propagate more modes, which interfere with each other and create wire-like, inhomogeneous patterns on the surface "Fig 6".

If compared to the SMC and adiabatic tapering, an arguably less complicated way to achieve a homogeneous sample illumination is actually using wide, highly multimode waveguides. As it will be discussed in the following section about the imaging setup, light is typically coupled through an objective focusing at the waveguide edge. Moving this focused spot along the edge leads to a modulation of the interference patterns, that, if averaged over this displacement, can also produce a homogeneous illumination of the surface. Despite putting requirements on the illumination section as well as possible longer image acquisition, this averaging approach gets rid of the SMC and tapering issues such as possible inhomogeneity at shorter wavelengths, long taper lengths (e.g. 2 mm for only 25 μm end width), and shadow effects on illumination through surface impurities.

Whereas the strong evanescent field is a must for single-molecule localization methods, techniques such as SIM or fluctuation-based nanoscopy algorithms profit from spatial frequency bandwidth given by the HIC. Structured illumination microscopy utilizes sinusoidal interference patterns for illumination, with the gain in resolution linked to the frequency of the interference pattern. Compared to the conventional SIM approach that uses a grating and a high numerical aperture objective to generate the patterned illumination, counter-propagating HIC waveguides can deliver higher frequencies of this interference pattern because of the high effective refractive index of the guided light. The advantages for fluctuation methods will be covered in the next section.

2.1.5 Multimode Waveguides and Super-Resolution

Whereas averaging of the multimode interference can be used to obtain diffraction-limited images, this modulation of the excitation intensity at the surface can also be combined with fluctuations based nanoscopy algorithms. Fluctuations based nanoscopy algorithms typically make use of natural variations in fluorescence emission of dyes [29, 8] to determine their position with higher accuracy than diffraction limited imaging, where the natural variations are averaged using sufficiently long exposure time and homogeneous illumination is assumed. This fluctuation in fluorescence emissions can also be induced artificially through inhomogeneous and time varying illumination patterns, such as speckle illumination [30].

In the case of HIC multimode waveguides, the high effective refractive indexes of the modes lead to higher spatial frequencies than achievable with objective-based optics in aqueous media. The "finer" patterns can be modulated, and therefore higher resolution can be obtained with waveguides compared to conventional setups. The UiT group has demonstrated this principle using an ESI algorithm (entropy-based super-resolution imaging) [4, 7], but a more dedicated

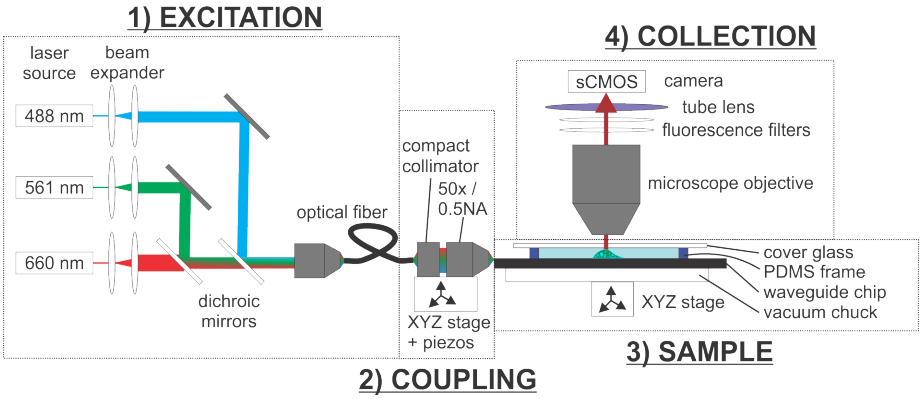

Figure 7: Scheme of chip-based microscopy setup.

illumination and image acquisition control can be used with other algorithms such as MUSICAL [8, 31] with a promise of better results.

2.2 Current Chip-Based Microscopy Setup

This section discusses the different parts of the setup as displayed in Fig. 7.

1. **Excitation:** Multiple lasers at typical bioimaging wavelengths, (e.g., 488, 561, 660 nm) are expanded as necessary, aligned to a common pathway and coupled into a fiber.

2. **Coupling:** Among the different possibilities to couple light into the chip (prism coupling, grating coupler, butt coupling with a fiber, direct focusing), direct focusing with a lens provides high efficiency by choosing a NA value similar to the waveguide's output with no necessary adjustments between different wavelengths through apochromatic optics. Given the dimensions of the waveguides used by the UiT group, previous work comparing different microscope objectives pointed towards the best efficiency with a 50x / 0.5 NA objective from Olympus (LMPLFLN).

   For the coupling unit, the end of the fiber with the excitation light is attached to a compact collimator (Thorlabs F280FC-A) with the output beam matching the back aperture of the coupling objective. Together with the coupling objective, those parts are mounted on a translation stage with piezo motors for precise positioning.

3. **Sample:** The waveguide chip rests on a vacuum chuck to prevent it from moving. The vacuum chuck itself is mounted on a translation stage. A chamber for biological specimens on the chip surface is made out of 150 µm thick PDMS polymer cut to a frame, filled with imaging media and sealed with a glass coverslip on top. The excitation light is focused onto a waveguide facet by the edge of the chip.

4. **Collection:** A modular microscope system from Olympus (BXFM model) collects the light from the chip. A revolving turret allows for quick

exchange of the imaging objectives. A white light source allows for reflective brightfield imaging of the sample. Filter slides for each excitation wavelengths which only allow the fluorescent signal to pass are exchanged as required. A scientific sCMOS camera (typically a Hamamatsu Orca Flash) records the images.

2.3 Multiple Signal Classification Algorithm (MUSICAL)

MUSICAL is a nanoscopy algorithm [8, 31] that generates super-resolution image of a distribution of fluorescent molecules (referred to as emitters) from a stack of microscopy images of fluctuations in intensity of the emitters. The principle of MUSICAL and the motivation of MUSICAL-on-chip are presented in the sub-sections below.

2.3.1 Principle

Using singular value decomposition of the stack of images, MUSICAL first partitions the mathematical space of the camera measurements into signal and noise sub-spaces. The signal subspace is spanned by the eigenimages corresponding to non-zero singular values and the null sub-space is spanned by the eigenimages corresponding to zero singular values. MUSICAL then computes an indicator function at every point of interest (PoI) in the sample space. This indicator function is the ratio of the projections of the point spread function (PSF) at the PoI on signal and noise sub-spaces.

MUSICAL was originally demonstrated to exploit blinking and bleaching phenomena of fluorescent molecules as the source of fluctuations in intensity. However, it is notable that the MUSICAL can exploit fluctuations in the illuminations as well. This is exploited in MUSICAL-on-chip, as described below.

2.3.2 MUSICAL-on-Chip

As illustrated before in Fig. 6, a multimoded waveguide generates complicated illumination patterns as a result of interference of waveguide modes. Also as previously mentioned, moving the focused spot that is used to couple the light into the waveguide across the width of the waveguide changes the net pattern by changing the amplitudes of different waveguide modes. A simple illustration is shown in Fig. 8. Therefore, the changing illumination patterns can be used as a mechanism to introduce fluctuations in a controlled manner, rather than relying on the stochastic phenomenon of photo-kinetics of fluorescent molecules. The photo-kinetics of fluorescent molecules imposes limitations on the choice of dyes, acquisition time and input power, which ultimately limit the signal to noise ratio of the measurement [29] and versatile application of super-resolution techniques, including MUSICAL. On the other hand, the ability to introduce fluctuations through illuminations created by photonic chip allows better control of signal to noise ratio and is therefore expected to make MUSICAL more versatile and dye independent. This is the motivation of MUSICAL-on-chip.

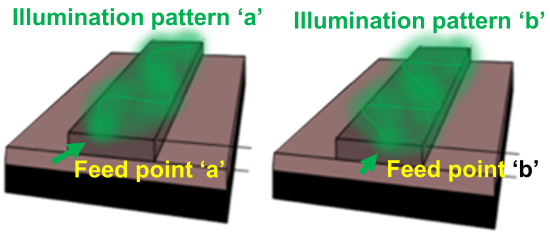

Figure 8: When coupling into wide multimode waveguides, different locations of feed point result in different illumination patterns.

In order to vary the illuminations in a systematic and efficient manner as well as to perform synchronized acquisition of image for each feed point, the following are needed:

1. Efficient coupling of light from laser into the waveguide
2. Precise control and stability of the feed point along the width of the waveguide
3. Integration of illumination system and image acquisition to enable synchronized and automated illumination switching and image acquisition

These objectives are achieved in this master thesis.

3 System Integration and Automation

This chapter presents the contributions of this thesis. As discussed in chapter 2, there was a need to design an integrated, automated, and synchronized set-up for coupling the light into the photonic chip efficiently, controlling the precision and stability of the feed point along the width of the waveguide, and acquire images in synchronism with the switching of illumination through shift of the feed point. The chapter presents the various activities undertaken to accomplish the target in the following sections.

3.1 Optimization of Illumination Set-Up of Current Chip-Based Microscope

As shown in the previous chapter, the waveguide setup has so far consisted of two translation stages (see also Fig. 7). This offered optimization potential in terms of size and cost. An alternative configuration, shown in Fig. 9, was co-developed with Postdoc Azeem Ahmad. Here, a precision milled aluminum mount fabricated at the department's machine shop can accommodate the necessary elements on top of a single translation stage (Thorlabs NanoMax).

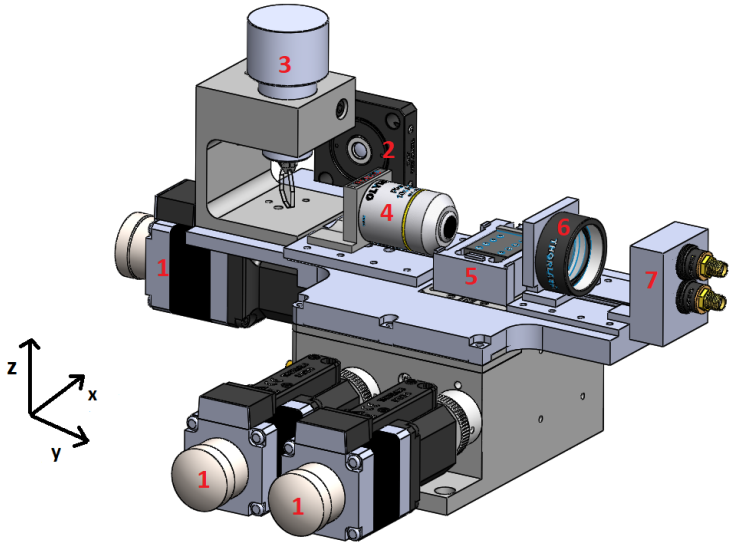

Figure 9: Alternative setup consisting of one translation stage with custom-designed aluminum mount, including motorized actuators (1) for the sample stage (5), integrated coupling section (2-4), and measurement system for automatic coupling adjustment (6-7).

The numeration in Fig. 9 corresponds to the following elements:

1. The coarse stage movement has so far been performed manually, but now motorized actuators for the three axes allow implementation of a feedback

system for automatic movement of the sample stage.

2. Compact fiber collimator. Micrometer precision of the aluminium mount removes the necessity of alignment towards the coupling objective.

3. Scanning mirror galvanometer. To achieve homogeneous illumination with multimode waveguides on the previous setup, the separate coupling stage oscillated over the x-axis using the piezo motor. The one axis galvo mirror greatly increases the oscillation frequency (130 Hz), reducing the necessary number of frames for mode averaging by almost 100 times.

4. Coupling objective mounted on a one axis long-range piezo motor (PI Q-522.140). The compact collimator can alternatively be mounted here, allowing for larger movements over the x-axis.

5. Apart from all other elements which are fixed to the aluminium mount, the vacuum chuck for the photonic chip is the only element resting on the moving section of the NanoMax stage. Coarse and fine movement in 3 axis is provided by the motorized actuators and the NanoMax's piezo motors, respectively.

6. Lens to collimate out-coupling and stray light for the photodiodes, discussed in this section.

7. Two photodiodes with focusing lenses. The obtained signal will be used in a feedback loop with the motorized actuators for automatic coupling adjustment.

Elements 6-7 from Fig. 9 were engineered to measure the light coming from the chip. The lower photodiode will only receive light which was guided by the chip (coupled light), while the upper photodiode will receive coupled light but also light exiting the coupling objective which is not stopped by or coupled into the waveguide (stray light). This is illustrated in Fig. 10.

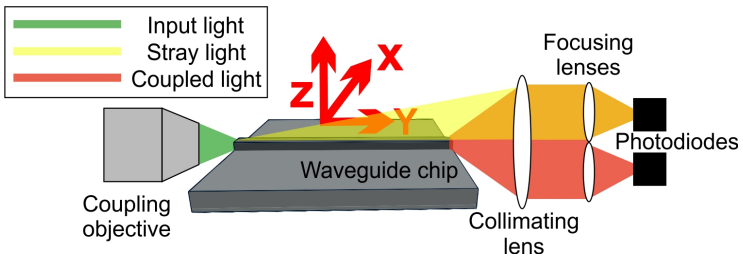

Figure 10: Scheme of photodiode assembly and types of light reaching each, generating the signal for the automatic coupling process. The axes definition represented here will be followed for the rest of this thesis.

The amplification of the light reaching the photodiodes is discussed in the following sub-sections and presented in Fig. 11. The signal in the upper photodiode can be used to locate the waveguide relative to the input beam before any coupling is achieved. How this is achieved will be the subject of section 3.2. The signal from the lower photodiode will be proportional to the power in the guided modes of the waveguide, hence also proportional to the coupling efficiency. This

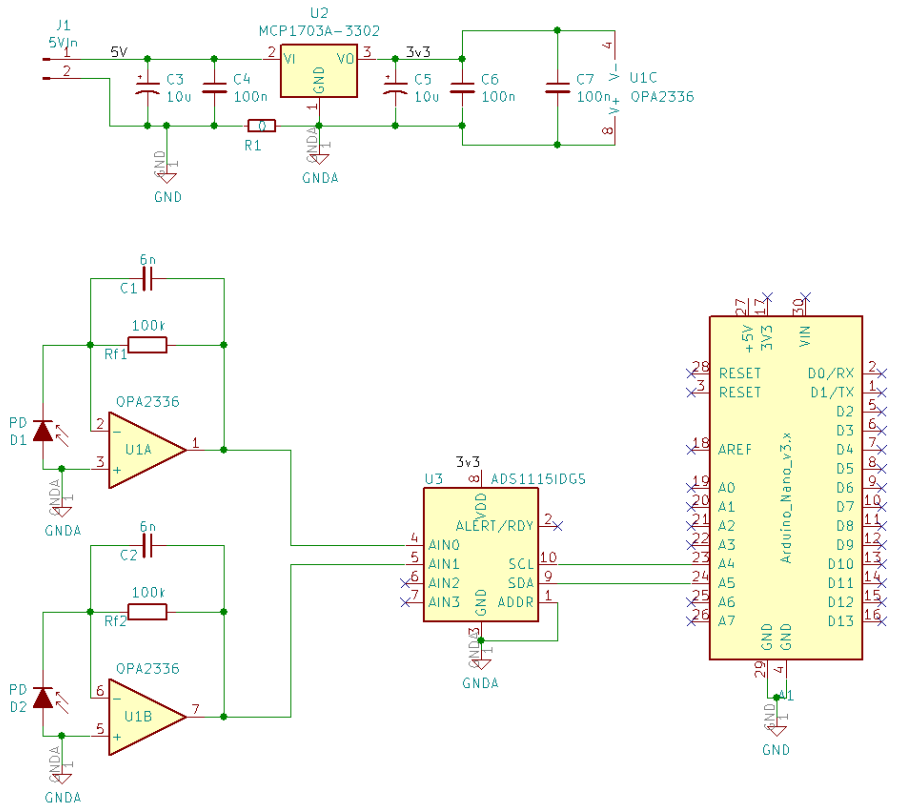

Figure 11: Schematic of setup developed to read the signal of photodiode pair. Top circuit shows a linear 3.3 V voltage regulator providing filtered power to the op-amps and ADC. Bottom circuit, from left to right: transimpendance amplifiers are connected to an ADC converter, which is connected to an Arduino.

is used to optimize the coupling as described in section 3.3. If not otherwise specified, all elements from the setup were purchased from Thorlabs. Fig. 9 and 10 display the axis definition which will be utilized for the rest of this thesis.

3.1.1 Photodiode Amplifier and Computer Interface

A system for amplifying and digitizing the photocurrent from the photodiodes shown in Fig. 9 and 10 was needed. As there was no comprehensive solution at a reasonable cost, it was decided to make a solution from three components. First, a transimpedance amplifier (TIA) amplifies the photocurrent generated by the photodiodes and keeps them biased at a constant voltage. Two amplifiers were connected to an ADS1115 analog to digital converter (ADC), whose digital signal was fed into an Arduino interface. The Arduino handles the control of the ADC through an inter-integrated circuit (IIC) interface, and exposes the functionality over a USB virtual com port at 2MBaud. The photocurrent may then be read out by a computer connected to the remaining waveguide setup

components. Fig. 11 presents the schematic diagram of the system including the power supply, the TIAs, the ADC and the Arduino.

3.1.2 Power Supply for TIA and ADC

The power to the system is provided through the 5 V supply provided by the USB. The USB power can however be a quite noisy source, so the components sensitive to noise, the TIA and ADC circuits, should not be directly powered by the USB power. Instead, the 5 V USB source is fed to a linear 3.3 V regulator which significantly reduces the noise. This is then used to power the TIA and ADC circuits.

3.1.3 Transimpedance Amplifier

The transimpedance amplifier converts a current to a voltage. The operational amplifier drives its output such that the voltage at the negative input is equal to that at the positive input. For that to happen, the current through the feedback network must be the same as the photodiode current. At DC, this requires $I_{pd} = I_{Rf}$, hence $V_{out} = R_f I_{pd}$. This converts the photocurrent to a voltage and provides amplification, while also keeping the diode at a constant bias of 0 Volts, which minimizes dark current and noise. The feedback capacitors limit the bandwidth of the amplifiers to reduce noise and prevent oscillation. The operational amplifier (opamp) Used is an OPA2336 [32], which has low input bias current, and low input noise, as well as rail to rail output capability. The feedback resistor is 100 kΩ providing a gain of 100 kV/A. The feedback capacitor is 6 nF giving a bandwidth of 265 Hz.

3.1.4 Analog to Digital Converter

The ADS1115 ADC was selected because it has good resolution of 15 bits in single ended mode operation. Further, it has a built-in voltage reference and a programmable gain amplifier supporting gains of 2/3 , 1, 2, 4, 8 and 16. This means that the system can be used for a wider range of input intensities without having to change the feedback network in the amplifiers. Finally, it is easily and cheaply available as a module, where the chip has been soldered to a breakout board, as well as an easy-to use-software library for the Arduino ecosystem [33].

3.1.5 Arduino and Firmware for Computer Interface

An Arduino is used to communicate with and control the ADC over an IIC interface. The functionality of the ADS1115 is controlled using a software library [33]. The required functionality is exposed to a host computer through a program running on the Arduino that accepts and interprets a set of commands. The communication between the Arduino and a host computer is through a USB virtual serial port. Further, a Labview library was implemented that handles the command based interface allowing easy integration with other components in a

Labview based environment. The Arduino firmware and the Labview interface are available in a github repository [34].

3.2 Initial Alignment

As it will be explored in the next section, waveguide coupling can be optimized through an algorithm but it requires some extent of initial coupling to be present. For coupling to occur, the waveguide and input beam must be aligned within a few micrometers. When considering the waveguide geometry, the width (x-axis) can range from a few to several hundreds of micrometers as opposed to the height (z-axis) of 150 nm. Disposing of a stage engineered with fine mechanical precision, a recurrent waveguide design can be accurately placed on the chip so that the necessary alignment of the waveguide width to the coupling spot is given. This reduces the initial coupling to be met through y- and z-axes, whereas the height is the first parameter which can be varied until initial coupling is obtained. The utilized NanoMax stage has the accuracy required to do so, but it exhibits significant crosstalk between the axes such that moving along the x-axis also moves the chip along the y- and z-axes [35]. This is a function of the mechanical structure of the stage, and may be compensated for if the crosstalk can be classified. This section presents an edge finding algorithm which may be used for initial coupling, but which was also used to classify the crosstalk between the stage axes.

3.2.1 Edge Finding Method

Assuming that the input beam is a Gaussian beam, the diameter of the beam varies along the optical axis as simulated in Fig. 12.

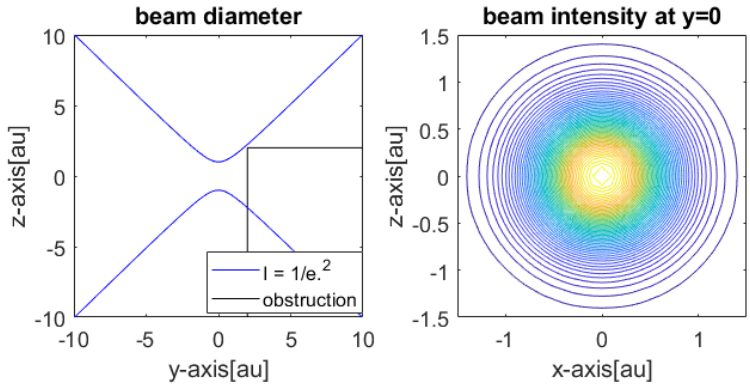

Figure 12: Left: Gaussian profile of the beam in the propagation direction. In black, obstruction symbolizing the waveguide edge placed in the beam path. Right: Intensity profile of the coupling beam at the focal spot (y=0).

If the beam were to be obstructed with a structure such as visualized, only the fraction of the beam above the structure would propagate past it as stray light.

If we collect and measure that light, the power of the light measured is given as

$$\int_{z_0}^{\infty}\int_{-\infty}^{\infty} I(x, y_0, z)dxdz, \tag{3}$$

where (y_0, z_0) is the position of top edge of the obstruction. By moving the obstruction, the measured power would then vary with its position.

Fig. 13(a) shows a calculation for this relationship between the $y-$ and $z-$axes. Out of the obtained curves it is evident that the chip edge (y_0, z_0) can be determined from the stray light's signal trend while alternatively moving the chip along the two axes.

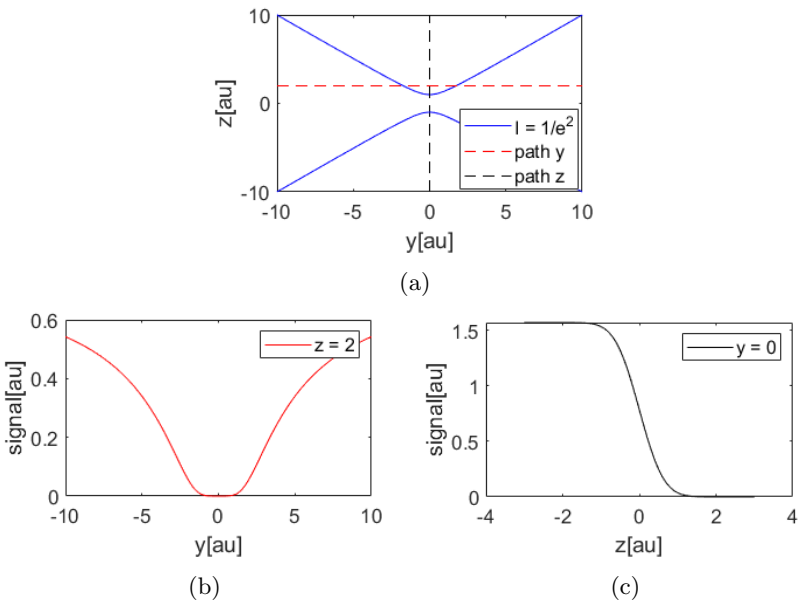

Figure 13: Simulation of stray light signal vs. chip edge position. (a) Gaussian beam profile (blue) with translated path of obstruction for y- (red) and z-axes (black). (b) Stray light signal for obstruction scanned over y-axis. (c) Stray light signal for obstruction scanned over z-axis.

For instance, by choosing an initial value of z and moving the chip along the y axis (red dashed line in Fig. 13(a)) while measuring intensity of the stray light, an intensity profile such as Fig. 13(b) can be obtained. The beam waist may then be found by selecting an appropriate threshold, the waist will then be located between the intersects of the intensity profile and the threshold. Once the beam waist has been found, the height of the beam relative to the chip may be determined by measuring the intensity profile while moving the chip along the z-direction (black dashed line in Fig. 13(a)), see Fig. 13(c). When the measured intensity is half the maximum value, the beam center would be aligned with the top of the chip.

This is of course a a simplified model. In a practical setup we cannot capture all the stray light. There are diffraction effects from the edge of the chip, interference between light reflected from the top of the chip with the light directly

propagating to the sensor, and the beam is not a perfect Gaussian shape. The result, as we will see, is similar but is not as symmetric and smooth as for the simplified model.

3.2.2 Implementation

A program performing the edge finding method was implemented in Labview and is available in a github repository [36]. The implementation largely following the procedure outlined in the previous section. Some changes had to be made to account for the imperfections of the real data used to develop the model, mainly the intensity profiles not being as nicely symmetric as in the idealized case. This means that the beam waist is not necessarily in the center between the intersections of the threshold and the intensity profile, but still somewhere between the intersections. Hence the accuracy of the method is limited. The procedure then follows the pseudocode presented in Listing 1.

1. Choose a point (y_0, z_0) such that waveguide chip is located above and to the left of beam waist
2. Measure stray light intensity $P_y = I_{stray}(y, z)$ for $z = z_0$, $y_0 < y < y_0 + \Delta y$ where Δy chosen large enough to give an intensity profile analogous to figure 14(b).
3. Estimate the beam waist y_w as the first and last elements of $P_y < I_{th}$ where I_{th} is a suitable threshold.
4. Get intensity profile $P_z = I_{stray}(y, z)$ for $y = y_w$, $z_0 - \Delta z < z < z_0$
5. Find estimate of waist along z-axis,z_w, as first element of $P_z < I_{th}$
6. Choose a new point (y_0', z_0') and $\Delta y'$ closer to the estimated waist.
7. Repeat point 2 3 to get y_w'
8. return (y_w', z_w)

Listing 1: Pseuodocode representation of edge finding method

The procedure was originally envisioned as an iterative procedure terminating when the measured z-profile indicated than a beam diameter became smaller than a given threshold. It was however found that subsequent iterations did not significantly improve the precision.

Experimental intensity profiles are presented in Fig. 14. The plot of the y-axis scan in Fig. 14(a) is analogous to the model in Fig. 13(b). It is taken with a scan resolution of 15 µm. As it can been seen, the asymmetry is strongly evident in practice. The subsequent scan in the z-axis depicted in Fig. 14(b) is analogous to the model in Fig. 13(c), also showing deviation from the smooth and monotonic variation of the ideal signal. It is taken with a scan resolution of 0.8 µm. This is followed by another scan in the y-axis with a finer scan resolution of 3 µm, shown in Fig. 14(c).

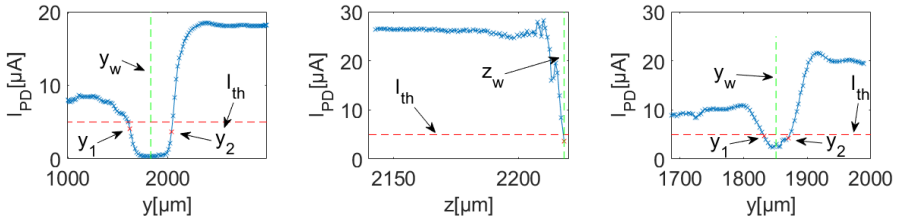

(a) First scan along y-axis (b) Scan along z-axis (c) second scan along y-axis

Figure 14: Experimental profiles of stray light signal scanned over (a) y-axis, (b) z-axis and (c) repeated for the y-axis, with indicated waists and thresholds. The asymmetry compared the ideal model from Fig. 14 and position refinement in (c) after optimizing the orthogonal axis in (b) are visible.

3.2.3 Stage Cross-talk Correction

Assuming that the chip is flat and its edges straight and smooth, the $y-$ and $z-$ axis commanded positions at different $x-$ values should represent a straight line in space. However, as previously mentioned, the crosstalk between the stage axes affects this trajectory. The corrupted translation has been measured through the stray light signal and is shown in Fig. 15. To obtain the values for the y and z axes separately, the edge-finding algorithm was performed for each x value.

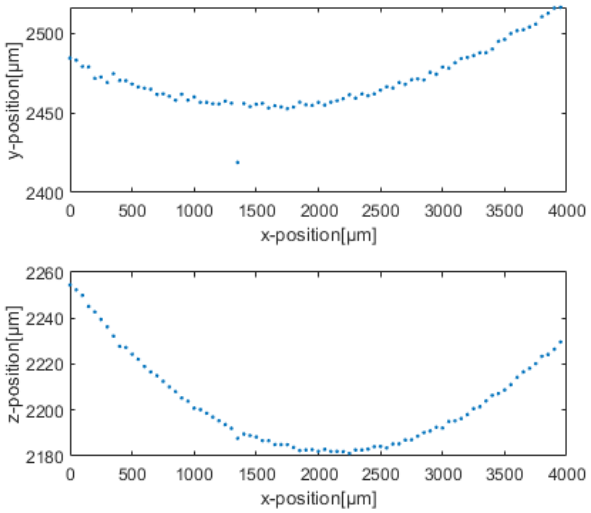

Figure 15: Translation of stage over x axis and its influence on y (top) and z (bottom) axes, measured through stray light signal. The non flat trajectory displays a crosstalk between the axes.

In order to model the effect of the crosstalk and to develop a way to compensate

for it, the affected trajectory between the axes can be modeled as:

$$x = x_c + f_{xy}(y) + f_{xz}(z), \tag{4}$$

$$y = y_c + f_{yx}(x) + f_{yz}(z), \tag{5}$$

$$z = z_c + f_{zx}(x) + f_{zy}(y), \tag{6}$$

where x, y, z are the true positions of the stage, x_c, y_c, z_c are the commanded positions, and f_{12} represents the dependence of axis 1 on axis 2. We cannot use this data to decouple the stage axes over the entire movement range. However, considering the intended use of the stage, it is enough to correct for it along the theoretical line from Fig. 15 as the beam waist should always be close to the top edge of the chip. To achieve this, we can neglect the crosstalk of y, z into x. Further we can assume that the true position of y and z is constant and approximately equal to the mean commanded positions $\bar{y}$ and $\bar{z}$, so that we obtain the following:

$$y \approx y_c + f_{yx}(x) \implies f_{yx} \approx \bar{y}_c - y_c \tag{7}$$

$$z \approx z_c + f_{zx}(x) \implies f_{zx} \approx \bar{z}_c - z_c \tag{8}$$

Using the data shown in Fig. 15, we can then find approximations of f_{yx} and f_{zx}. Fig. 16 shows plots of the data along with fitted 3$^{\text{rd}}$ order polynomial functions using the least squares method. The residuals of the fit are also shown in the figure. The constants of the polynomials as well as the root mean square error (RMSE) of the fits are presented in Table 1. Whereas the crosstalk measurement indicates that the position deviation can reach up to ca. 70 µm for the $y-$ and $z-$axes, as noted in Fig. 15, the results show that a correction based on the fit can keep the x-translation constant a range of less then 2 µm ($y-$axis) or less than 1 µm ($z-$axis), as seen in Table 1.

Fitted polynomial	RMSE
$f_{yx} \approx (1.295 \cdot 10^{-10}x^3 - 1.210 \cdot 10^{-5}x^2 + 3.703 \cdot 10^{-2} - 11.63)$µm	1.423 µm
$f_{zx} \approx (4.719 \cdot 10^{-10}x^3 - 1.831 \cdot 10^{-5}x^2 + 7.149 \cdot 10^{-2}x - 52.59)$µm	0.6103 µm

Table 1: Approximations to crosstalk compensation functions

It should be noted that the crosstalk correction relies in a reproducible position of the chip over the y-axis when placed on the sample stage. As a preliminary solution to guarantee reproducible placement, a part of a snap-away utility knife blad was bonded to the vacuum chuck with cyanoacrylate glue, shown in Fig. 17. The height of the blade was adjusted so that the typically 1 µm thick chip could be pushed against this "fence" without it reaching to the top of the chip blocking the coupling beam.

3.2.4 Conclusion about initial alignment

The edge-finding process was originally conceptualized to be performed when changing between waveguides of the same chip. However, components such as

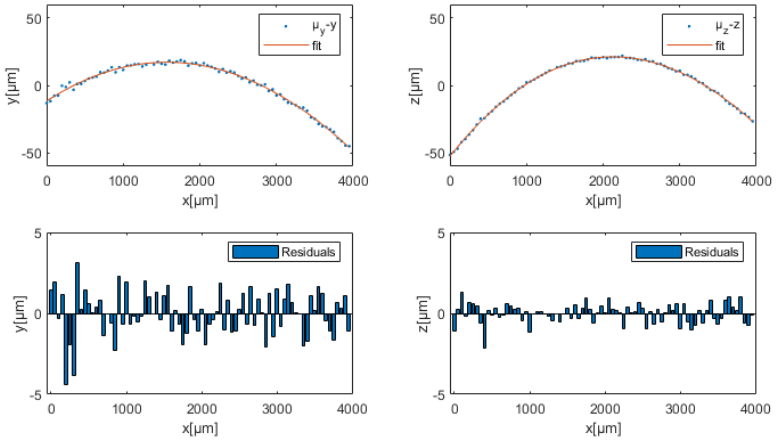

Figure 16: Linear least squares-based polynomial fit of stage crosstalk for y- (top left) and z-axes (top right) when translating the x-axis, including residual values for the fit (bottom plots).

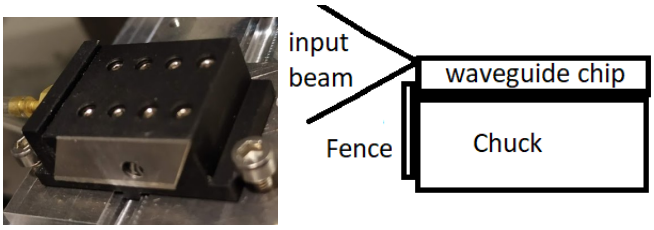

(a) (b)

Figure 17: (a) Metal piece ("fence") attached to chip holder allowing for repeatable placement of chip in the y-axis. (b) Scheme of side view showing the fence's placement so that it does not interfere with the coupling beam.

PDMS frame and glass coverslip would disturb the process as they can also diffract/guide some of the stray light. Characterizing and compensating for the crosstalk of a given stage combined with a method off repeatably placing the input facet of waveguide in the region where the compensation is valid, should suffice to guarantee a linear translation between different waveguide inputs, so that a constant height and thus initial coupling should be kept over the width of the substrate when only manually aligning over the $x-$axis, which is easily achieved with a micrometer stage.

3.3 Automated Optimization of Coupling Efficiency

The motivation to an automatized coupling system was mentioned at the very beginning of this thesis. To quickly review it, such a solution will obviate the need of manual coupling process and will provide a quicker, more predictable and reproducible optimization of the illumination intensity. This will cut down the

demands of user expertise as well as the time taken for light coupling and thus photodamage of the sample. As the previous section worked towards providing an initial coupling, this section continues on how to maximize the coupling efficiency using automated instrumentation.

3.3.1 Measuring the Coupling Efficiency

Different possibilities can be thought of on how to monitor the light coupled into the waveguide. One strategy is to use the imaging camera shown in block 4 of Fig. 7 to collect the light, which would have the advantage of not requiring additional hardware. The signal to be worked with could be fluorescence, autofluorescence or scattered light. However, without additional components, monitoring coupling would not be possible independent of imaging. An alternative would be to utilize an additional laser, e.g., in the near infrared range, coupled to the waveguide and additional optics at the imaging microscope leading the signal to a separate photodetector.

Section 3.1 has shown the strategy that was developed for the detection. Utilizing photodetectors to capture out-coupled light at the chip's rear end presents advantages for the acquisition process, finally being faster, less noisy (larger area detector, less gain needed) and allowing continuous measurement of the coupling without interfering with the imaging light path. On the negative side, making use of out-coupled light sets demands on the waveguide geometry. For example, it necessitates an out-coupling arm. This can however be easily implemented at structure design level through a waveguide splitter with one arm crossing the chip length to its rear end.

3.3.2 Process Concept

By using direct focusing, optimizing the coupling efficiency becomes a problem of alignment. If assuming constant excitation wavelength, waveguide dimensions and coupling optics, the coupling efficiency η becomes a function of the coupling objectives' position x, y, z. Further, if considering multimode waveguides with widths that are orders of magnitude larger than the height of the waveguide, the x-axis should not be considered as a degree of freedom when optimizing the coupling efficiency. The problem is then reduced to adjusting the alignment of the excitation beam and the waveguide along the $y-$ and $z-$axes such that the coupling is maximized.

In order to get an idea of how the coupling efficiency depends on the displacement of the excitation beam with respect to the waveguide, the following experiment was conducted. Using a setup similar to that of Fig. 9, but with manual screws rather than stepper motors, the piezo actuators were set to the middle of their range. The alignment was then manually adjusted until the coupling efficiency measured as the outcoupled light through the photodiodes was close to the maximum. The intensity of the light coupled into the waveguide was then measured over a grid of 200 X 200 steps over the range of the piezo motors (20 µm). The result is presented in Fig. 18. This can give an idea of the accuracy required to optimize the coupling, for example in order to get within

90% of maximum we need to get the placement of the coupling objective within a rectangle of about 2 µm × 0.2 µm.

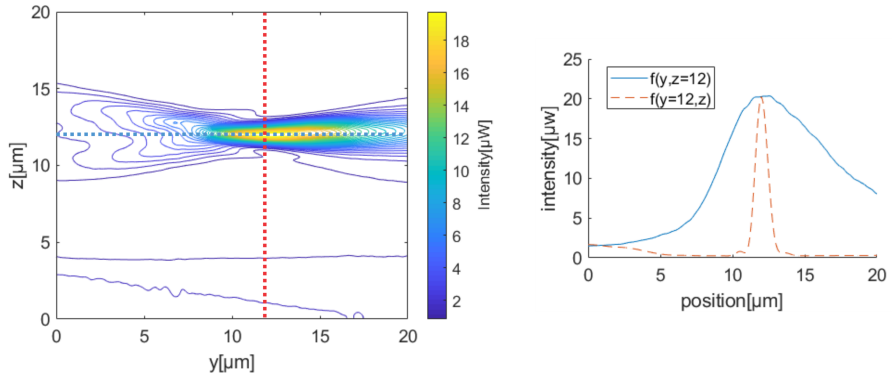

Figure 18: Left: coupled light signal measured as function of coupling objective's relative position. The sectioned lines go through the maximum for each axis. Right: plot of sectioned lines marked in the left graph, clearly showing the asymmetry between the axis.

3.3.3 Method 1: Gradient Descent

Gradient descent algorithm is a first-order iterative optimization [37] which is commonly used because it has good convergence rates for many problems as well as is easy to understand and implement. The gradient of a smooth function will point towards a point where the function has a higher value, given it is not at a stationary point. Thus, to maximize a function $f(y, z)$ one can move in the direction of the gradient. For a suitable step size α and given a starting point $\mathbf{x}_0$, a better point $\mathbf{x}_1$ can be found by as:

$$\mathbf{x}_1 = \mathbf{x}_0 + \alpha \nabla f(\mathbf{x}_0) \tag{9}$$

In the case that the analytical gradient is not available, we can use a numerical approximation as below:

$$\nabla f(y, z) \approx G(y, z) = \frac{f(y + h, z) - f(y, z)}{h}\hat{\mathbf{y}} + \frac{f(y, z + h) - f(y, z)}{h}\hat{\mathbf{z}} \tag{10}$$

In general, the step h used in the approximation should be small in order to get good accuracy. However, in practice, noise must be expected in the measurements. Given an underlying ideal or "ground truth" function f, we can say that we have access to the measurement function $\hat{f}$:

$$\hat{f} = f + \mathbf{X}(\mu, \sigma) \tag{11}$$

Where $\mathbf{X}$ is a random variable of mean μ and standard deviation σ. $\hat{f}$ is defined here to be $\ln P$, where P is the power in Watts (W). Given that f is a function

of position, while $\mathbf{X}$ is not, we can see that choosing a small value of h tends to amplify the influence of noise on the approximated gradient. On the other hand, choosing the value of h too large results in an inaccurate approximation of the gradient. Further, as can be seen in Fig. 18, the coupling efficiency is highly dependent on the dimension it is measured along. This implies that the step used in the approximation should also depend on the dimension it is taken along. To account for this, we introduce asymmetry in the step such that $\mathbf{h} = h_y\hat{\mathbf{y}} + h_z\hat{\mathbf{z}}$, and the approximated gradient is given as:

$$\nabla f(y,z) \approx G(y,z) = \frac{\hat{f}(y+h_y,z) - f(y,z)}{h_y}\hat{\mathbf{y}} + \frac{\hat{f}(y,z+h_z) - f(y,z)}{h_z}\hat{\mathbf{z}} \tag{12}$$

The step size parameter α, is very important for the performance of the steepest descent method of optimization in that it determines the convergence properties of the method. An α too small yields slow convergence, while an α too large will cause the algorithm to make steps too large, such that it does not converge at all, rather it will oscillate around a local minimum. The optimal step size is highly dependent on the cost function used, and generally a fixed step size is not ideal. There are methods that can be used to continually adapt the step size to the cost function. Perhaps, Barzilai-Borwein method [38] is the most common among them. This however is an approximation to a quasi-Newton method, which means it uses the approximation of second order derivatives. As previously discussed, derivatives of noisy functions tend to amplify the noise, and higher order derivatives will tend to amplify it even more. Further, it is necessary to limit the step size when optimizing functions with considerable noise, because making a large step with the cost function will tend to move to a region where no signal is present.

For these reasons, a fixed step size is used. However, We do introduce a non-isotropic step size such that $\alpha = \alpha_y\hat{\mathbf{y}} + \alpha_z\hat{\mathbf{z}}$ on similar reasoning such as used for $\mathbf{h}$. As the rate of change of the objective function is highly non-isotropic with $\frac{\partial f}{\partial y} << \frac{\partial f}{\partial z}$, the value tends to be limited by the movement along the $z-$axis when using a scalar step size. Therefore, it will tend to overstep and/or oscillate along this dimension, while only slowly converging along the $y-$axis. Introducing the non-isotropic step size parameter, it is possible to avoid this behaviour.

The termination criterion used in steepest descent optimization is usually such that it terminates when $|G(x)| < \epsilon$, where ϵ is a cutoff value chosen to achieve the required precision. When noise is involved, this method is not reliable. In this case, the termination criterion is chosen such that it terminates when the path length taken in an interval Δ_n iterations is below some threshold ε, such that $||\mathbf{x}_n - \mathbf{x}_{n-\Delta n}|| < \varepsilon$ or until a maximum number of iterations n_{max} have been executed. A pseudocode representation of the adapted algorithm is shown in Listing 2.

```
n = 0
while  n < n_max
    s_n = α_y G_y(x_n) ŷ + α_y G_z(x_n) ẑ
    x_{n+1} = x_n + s_n
    if  ||x_n − x_{n−Δn}|| < ε
```

```
            return x
        n = n + 1
```

Listing 2: Pseudocode representation of modified gradient descent algorithm.

3.3.4 Method 2: Nelder-Mead Simplex Algorithm

Nelder-Mead simplex is a direct search algorithm that can be used to find local minima or maxima of a function. For an n-dimensional problem it works by creating a test of set points arranged as an (n+1)-dimensional simplex, and comparing function's values at the vertices to replace the worst vertex by a better one. In searching for the better vertex, it follows a set of rules to determine where to look for it [39, 40]. A block diagram representing the algorithm is presented in 19, where f, x_0, γ, β are the function to be minimized, the starting point, the expansion coefficient and contraction coefficient, respectively. The function f used here is the power in microWatts (μW)

In the algorithm, the initial simplex $\mathbf{S} = \{\mathbf{x}_0, \mathbf{x}_1, \cdots, \mathbf{x}_n\}$ is constructed using the starting point as the first vertex, and generating the other vertexes such that $\mathbf{x}_i = \mathbf{x}_0 + h_i\hat{\mathbf{x}}_i$ for $i \in \{1, 2, \cdots, n\}$, where h_i determines the size of the initial simplex and $\hat{\mathbf{x}}_i$ are unit vectors. The expansion and contraction coefficients, γ, β, determine how much the simplex is expanded or contracted depending on the appropriate action determined by the algorithm. Heuristically chosen standard values used are 2 and 0.5, respectively. In general, the optimal choice of initial simplex size and coefficients depends upon the function f and is generally difficult to determine. The termination criterion is generally such that the process is terminated when the simplex shrinks below a certain threshold. This could, for example, be the average distance from the center point of the simplex to the vertexes.

3.3.5 Performance Simulation - Without Noise

In order to evaluate the performance of the optimization approaches, a model representing the coupling efficiency as function of displacement was made based on the data used to create Fig. 18. This data presents noise stemming from the measurement process, which however manifests as a static pattern in the model. Therefore, it does not model the behaviour of a real system with sufficient complexity. This static noise was reduced by applying a low pass filter to the data. Following it, a piece-wise linear interpolation was used to create a continuous objective function, f_{obj}, that can be used to simulate the performance of the optimization approach. The function f_{obj} was suitably modified for the definition of $\hat{f}$ or f of the two algorithms.

Fig. 20a (gradient descent method) and 20b (Nelder-Mead simplex algorithm) show the path of the procedures when applied to this model at 10 different starting points. Fig. 20c and Fig. 20d show the function value progression for the two methods respectively as the iterations proceed. Here, both approaches were run for 100 iterations. It is apparent that both approaches successfully improve the simulated coupling efficiency in almost all the cases, while getting

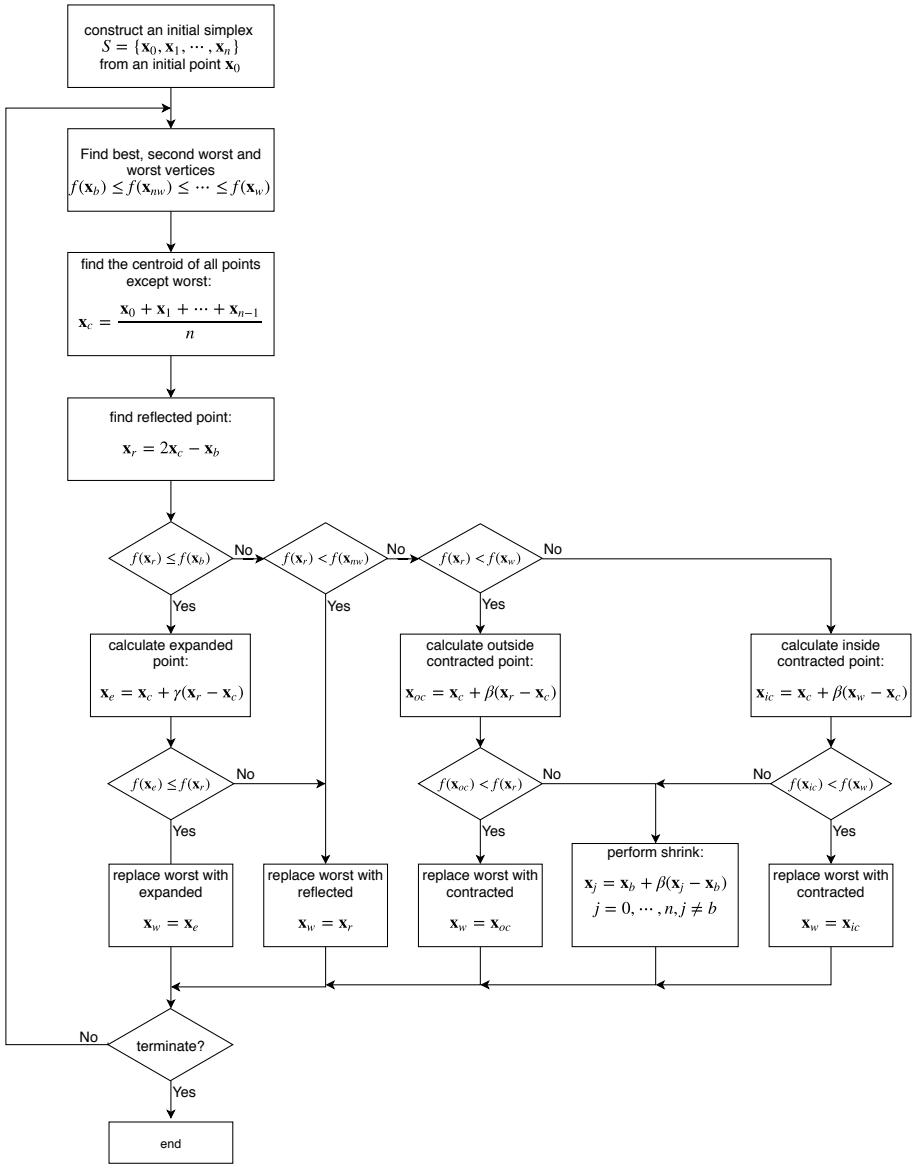

Figure 19: Block diagram illustrating the Nelder-Mead simplex algorithm.

stuck in local minima for one case in the gradient descent method and two in the Nelder-Mead simplex algorithm.

3.3.6 Performance Simulation - Including Noise

To get a more realistic sense of the average performance of the optimization algorithms, they were applied to the measured data with different levels of noise added to it. The simulation was performed for 1000 different starting points

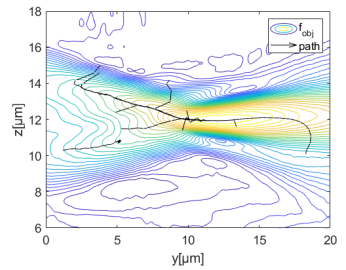

(a) Gradient descent

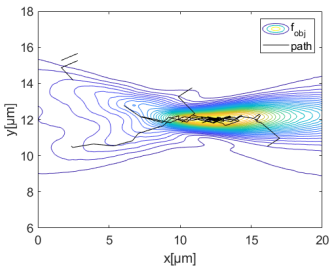

(b) Nelder-Mead simplex

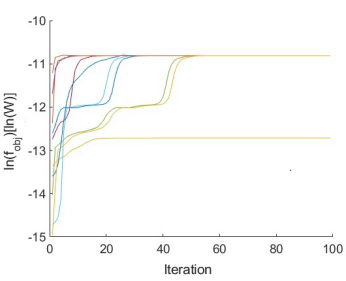

(c) Gradient Descent

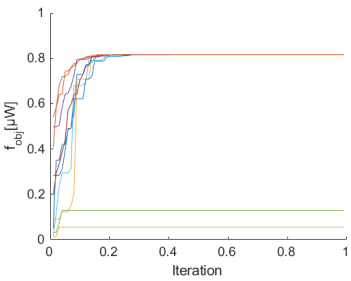

(d) Nelder-Mead simplex

Figure 20: Using the measured coupling efficiency from Fig. 18, simulations show the path taken for 10 different starting positions at 100 iterations (black) for the gradient descent algorithm (a) and Nelder-Mead simplex algorithm (b), including the evolution of the function value for both (c, d).

within the region shown in Fig. 21. This considered area was determined by taking $f_{obj} > 1.8\mu W$, further excluding 1 µm from the edges.

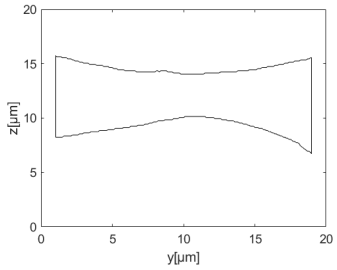

Figure 21: Contour of region of measured data selected for simulations including noise.

The number of points ending in a successful result were recorded, this being defined as objective function values within 90% of the maximum. The start (black circles) and endpoints (red dots) are shown in Fig. 22 and 23, with the results presented in Table 2. In Table 2, σ_n is the standard deviation of the noise added expressed in percent of the maximum value of f_{obj}, N_s is the number of starting points that resulted in success, μ_i is the average number of iterations before termination, α is the step size used in the gradient descent algorithm and

β is the contraction coefficient used in the Nelder-Mead simplex algorithm. The expansion coefficient γ is kept at 1.3 in all cases for the Nelder-Mead simplex algorithm.

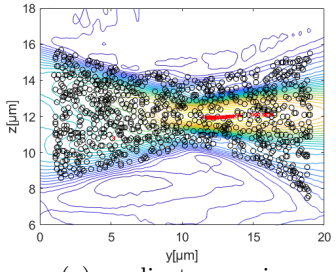

(a) gradient, no noise

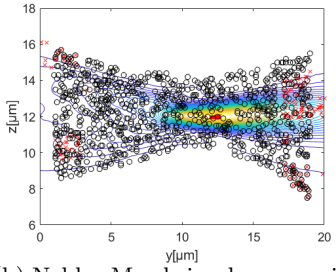

(b) Nelder-Mead simplex, no noise

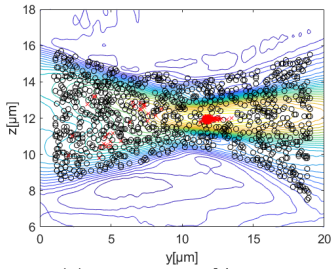

(c) gradient, 1% noise

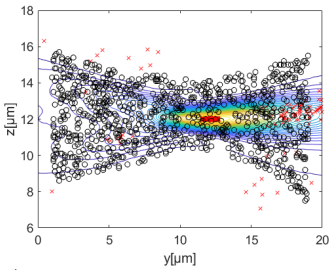

(d) Nelder-Mead simplex, 1% noise

Figure 22: Performance of optimization algorithms on simulated dataset, 0-1% added noise. Black circles show the starting points, red circles the end points.

σ_n	0%	1%	5%	10%
N_s	781	792	667	202
μ_i	48.6	45.9	53.7	56.9
α_y	3	3	1	1
α_z	0.3	0.3	0.1	0.1

(a) Gradient descent method

σ_n	0%	1%	5%	10%
N_s	825	904	827	766
μ_i	34.6	37.8	50.5	69.1
c_{con}	0.5	0.7	0.8	0.85

(b) Nelder-Mead simplex algorithm

Table 2: Results from simulations shown in Fig. 22 and 23.

As indicated by the results, the Nelder-Mead simplex algorithm has superior performance in terms of average number of iterations until termination as well as a higher number of successful outcomes when used on the simulated dataset. In both cases it is advantageous to tune parameters according to the noise level. For the Nelder-Mead simplex algorithm, the most important parameter is the contraction coefficient β. The Nelder-Mead simplex algorithm tends to favour the contraction and shrink transformations over reflection and expansion as the noise level increases, probably because there are more outcomes where these actions will occur. In this case, as the noise level increases, the transformation selected is more randomly chosen and it seems reasonable that the simplex tends to shrink. Limiting the shrinking then allows something akin to an oversampling of the objective function, allowing it to get closer to an optimal position before

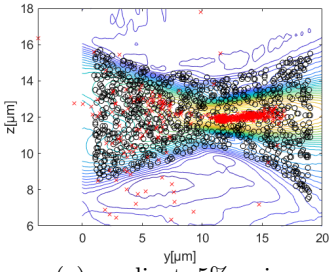

(a) gradient, 5% noise

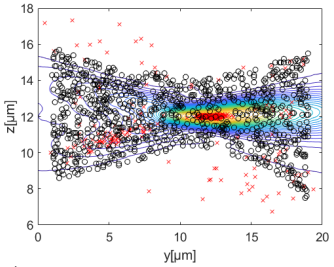

(b) Nelder-Mead simplex, 5% noise

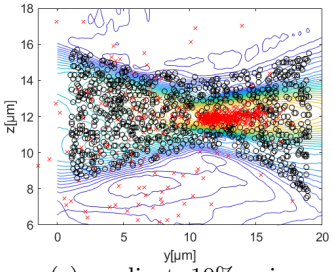

(c) gradient, 10% noise

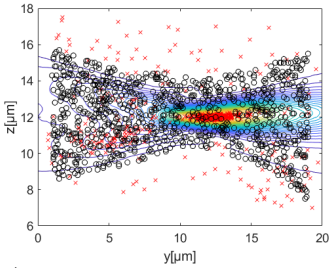

(d) Nelder-Mead simplex, 10% noise

Figure 23: Performance of optimization algorithms on simulated dataset, 5-10% added noise. Black circles show the starting points, red circles the end points.

terminating, at the cost of a slower procedure.

For the gradient method it is also beneficial to decrease the step size α. As the noise level increases, the gradient descent method changes from moving along the gradient to a random walk biased to move in the direction of the gradient. Using a too large step size increases the likelihood that a large step is taken such that the optimization procedure ends up in a region where the objective function is flat with only noise is present. The performance of the gradient optimization procedure is also limited by the termination criterion used. The method used tends to terminate prematurely, but the number of successful runs increases significantly if based on a fixed number of iterations. Optimization towards terminating the procedure could therefore provide better results, with the fixed number of iterations method not been seriously considered.

3.3.7 Conclusion and Implementation

Based on the results from the previous section, the Nelder-Mead simplex algorithm was chosen as the better candidate for performing automated coupling optimization. It was implemented as part of a Labview program available at a github repository [36]. Here, the user is presented with an interface as shown in Fig. 24. The workflow of the system is as follows:

1. A waveguide chip is placed on the vacuum stage, making sure that it is located against the fence on the chuck.

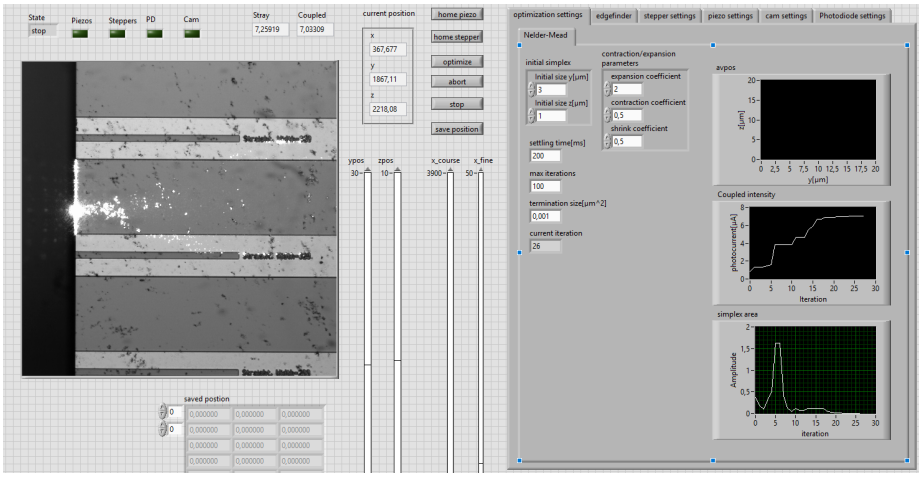

Figure 24: Labview interface of implemented automated coupling optimization.

2. The waveguide that is to be coupled into is located using the microscope.
3. The laser is turned on, an manually aligned with the waveguide using the x-axis slider. Because of the stage crosstalk correction this should then provide initial coupling.
4. The optimization procedure can then be started by pressing the "optimize" button.

The automated optimization of coupling as implemented has not been thoroughly tested, however initial testing is promising. Given adequate initial coupling, the program consistently improves the coupling efficiency. In most cases it was found not possible to further improve the coupling efficiency by manually adjusting the stage position, but the automation did in some cases get stuck in local minima. In some cases it was possible to simply run the optimization procedure again after it had terminated in a local minimum, though in other cases manual adjustment of the starting point was required. On the right hand side of Fig. 24, the result of a single optimization procedure is visible where the initial coupling induced a photocurrent of ~ 1 µA (corresponding to an intensity of ~ 3 µW) which was improved by the automatic optimization procedure to ~ 7 µA (~ 21 µW) in 27 iterations, or roughly 11 seconds.

3.4 Controlled Multimode Illumination

3.4.1 Motivation

As discussed in section 3.2.2, precise control of the beam scanning the input width of multimode waveguides can take fluctuation-based super-resolution algorithms such as MUSICAL to a new level. Chip-based fluctuation demonstrated so far made use of a continuous, asynchronous movement of the coupling objective towards image acquisition [4]. To most effectively utilize the

multimode nature of the illumination, a fully controlled movement in a stepwise acquisition manner should be provided. This way, the spatial frequencies acquired can be assumed to the highest through the stable illumination. The presented work so far focused in optimizing the coupling efficiency. From here on, the attention will be put towards the mechanism to control the illumination over the waveguide width.

3.4.2 Methodology

The following equation modeling coupling to a waveguide mode may give some insight to the related variables [41]:

$$\eta_m = \frac{\left[\int\int \vec{E}_{ex}(x,y)\vec{E}^*_{wg_m}(x,y)dxdy\right]^2}{\int\int \vec{E}_{ex}(x,y)\vec{E}^*_{ex}(x,y)dxdy \int\int \vec{E}_{wg_m}(x,y)\vec{E}^*_{wg_m}(x,y)dxdy} \tag{13}$$

where $\vec{E}_{ex}$ is the electric field of the excitation light at the waveguides input facet and $\vec{E}_{wg_m}$ the electric field of a mode m that the waveguide supports. η_m is then the coupling efficiency of the excitation field into that mode. It is then apparent that a given $\vec{E}_{ex}$ will couple a given amount of power into the m different fields supported by the waveguide. By changing $\vec{E}_{ex}$ we will also change the associated coupling efficiencies η_m.

There are several possible ways to modulate the illumination pattern of the waveguide, e.g., galvanometers, spatial light modulators, linear stages. For random averaging of the modes it was acceptable to scan the beam onto the coupling objective's back aperture. With, e. g., a galvanometer the beam oscillation will be very fast, but the scanning spots will be asymmetric through the skew beams at the objective's back aperture. To provide the best beam quality, a scanning stage carrying the exciting laser coming from a fiber together with the collimating optics and the coupling objective should provide the most flexible option with the best beam quality. For this stage, a travel range of at least 1 mm with a resolution below 10 nm would be ideal. Those requirements were met by the one dimensional linear stage Q-522.140 from Physik Instrumente (PI), claiming a travel range of 13 mm and a sensor resolution of 4 nm. The resolution, stability and other characteristics will be characterized in this section.

3.4.3 Mode of Operation

The Q-522.140 motor works by a carriage mounted to a block with an actuator coupling them through a friction pad. The preload and actuator are selected such that a suitable acceleration can be produced, and the actuators force generating capability is high enough to overcome the friction. This enables principally unbounded movement of the carriage by slowly extending the actuator and rapidly retracting it, repositioning the friction pad with each rapid retraction ("stick slip" system). The drive mechanism is illustrated in Fig. 25.

Applying a sawtooth waveform to the actuator will produce continuous motion in the stage. It may further be operated as a conventional piezoactuator, where

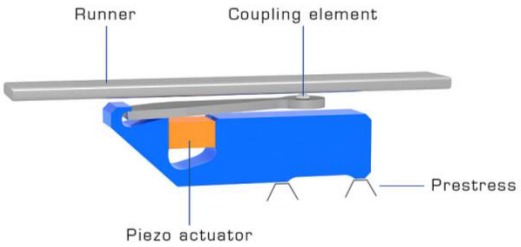

Figure 25: Stick-slip drive mechanism [42].

the actuator contracts approximately linearly with applied voltage. Combined with a suitable displacement sensor and controller, such a system can achieve high positioning accuracy over a large range of motion.

3.4.4 Tuning the Control System

The stick slip stage control system is steered using the E-873 controller from PI. The E-873 follows a hybrid strategy using feed-forward control during rapid movement and shifts to PID-based control when doing final positioning. When in feed forward mode, a sawtooth wave is applied to the actuator. The difference in slope of the waveform provides forces lower then the static friction of the pad to move forwards, then rapidly contracting to overcome the static friction when retracting the actuator.

Tuning the system involves adjusting the parameters made available through the API (application programming interface) presented by the E873 controller. The E-873 is apparently identical to the E-871 system shown in Fig. 26. The relevant parameters in this case are the gains in the proportional-integral-derivative (PID) algorithm (K_p, K_i, K_d) and the notch filter center frequency (f_0) and width. The width of the filter is represented by a dimensionless number between 0.1 and 10, inversely proportional to the actual filter width.

The PID algorithm itself is as follows:

$$u(t) = K_p e(t) + K_i \int_0^t e(t)dt + K_d \frac{de(t)}{dt} \tag{14}$$

Where $u(t)$ is the output and $e(t)$ is the error, or the difference between set point and actual position. Tuning a PID servo control can be done by first developing a dynamic model of the system being controlled (piezo motor and load) and then including the controller itself in the model. A transfer function representing the control system (stage and controller) can then be found and appropriate values of K_p, K_i andK_d set to yield the desired system response within the limits determined by the dynamics of the system. Making an accurate model of the system can however be difficult and time consuming. In this case, many parameters concerning the dynamics of the stage are unpublished (stiffness, damping, capacitance, resistance etc.), which complicates the creation

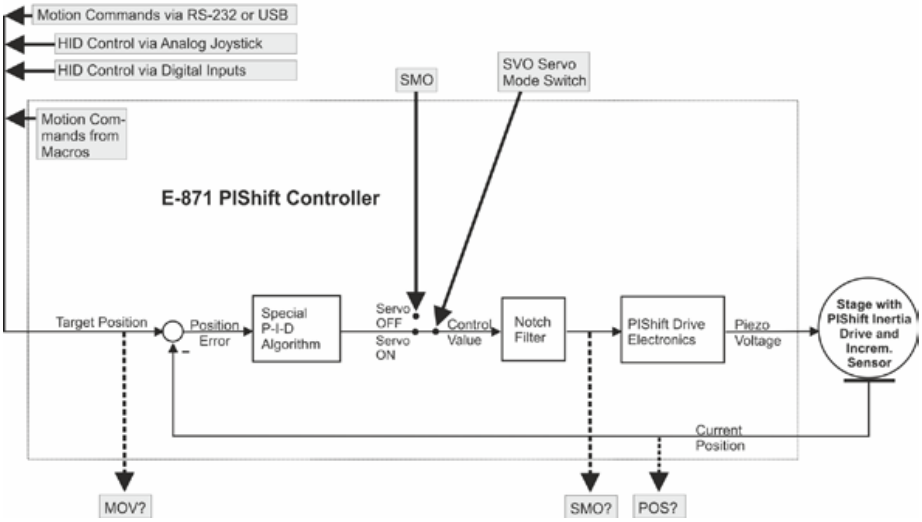

Figure 26: Control algorithm for the PI Q-522.140 stage [43].

of a precise model. However, having a general sense of the effect of each PID coefficient on a general system, the parameters may be tuned heuristically. The general effect of increasing the parameters of a PID loop is outlined in Table 3 [44].

Param.	Rise time	Overshoot	Settling time	Stdy. state err.	Stability
K_p	Decrease	Increase	Small change	Decrease	Degrade
K_i	Decrease	Increase	Increase	Eliminate	Degrade
K_d	Increase	Decrease	Decrease	No effect	Increase

Table 3: Effect of increasing Proportional, integral and derivative gains K_p, K_i and K_d

Note that in some cases where there is noise in the measurement of the process variable, the derivative term is unusable. Typical additive noise will manifest as a high frequency component in the signal, which is effectively amplified by the high pass filtering properties of the derivative. In such cases, adding the derivative term will tend to degrade the system performance.

The notch filter depicted in Fig. 26 is not a part of a standard PID-loop but can be used to enable the use of higher gains in the controller, allowing improved settling time of the system. If there are resonant modes in the system being controlled, these will manifest as spikes in the frequency response. As there is also a phase shift associated with these spikes, positive feedback may occur in these regions causing oscillation. By introducing the notch filter at the same frequency as that of the resonant mode, spikes in the frequency response may be compensated for. This will then allow to increase the proportional and integral gains, improving system response time.

Starting the controller using the factory settings caused alarming oscillations to

occur. The resonant frequency of this oscillation was found by setting the controller to open loop mode, commanding a step change in position, and recording the response of the stage. A discrete Fourier transform was then applied to the the data and the resonant peak was found at a frequency of 170 Hz, shown in Fig. 27.

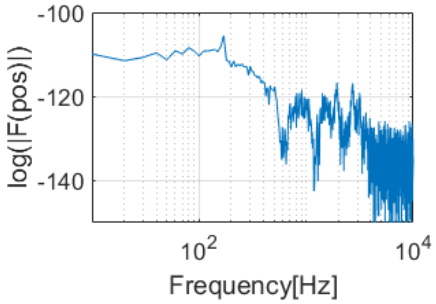

Figure 27: Open loop step response in frequency domain of PI stage, showing a resonant peak at 170 Hz.

The notch filter center frequency f_c was then set to the frequency of these oscillations. The filter width f_w is set by a number w such that $0.1 \leq w \leq 10$ that is inversely proportional to the width of f_w. Using a relatively wide filter $w = 1$ seemed to decrease stability of the system, while using a narrower filter (that is, a higher w value), reduced the tendency to oscillate somewhat. By trial and error, a value of $w = 8$ seemed to provide the best improvement to the system response.

The filter somewhat improved the stage response, but it still tended to oscillate sporadically, seemingly dependent on position and travel direction of the last commanded position change. Attempting to improve stability by setting $K_d > 0$ made for an unstable system with large amplitude oscillations, indicating that the position feedback signal is too noisy to allow use of the derivative term. The K_p and K_i parameters then had to be lowered in order to stabilize the control system. Table 4 shows the factory default parameter set and the final settings determined to provide a stable system response.

	K_p	K_i	K_d	f_c	f_w
factory settings	30	8000	0	-	-
final settings	10	2000	0	170	8

Table 4: Control loop parameters for the PI-stage controller, comparing factory default settings and settings found to produce a stable system response.

3.4.5 Sensor Noise

The sensor noise was estimated by turning off the position control system and reading out the position for 10000 samples at an acquisition rate of 20 kHz. As the control loop is not engaged, any noise in the data should be due to noise

from the encoder. Fig. 28 shows a histogram with the deviations from the set-point for this. A standard deviation of 4.6 nm was calculated from the obtained values.

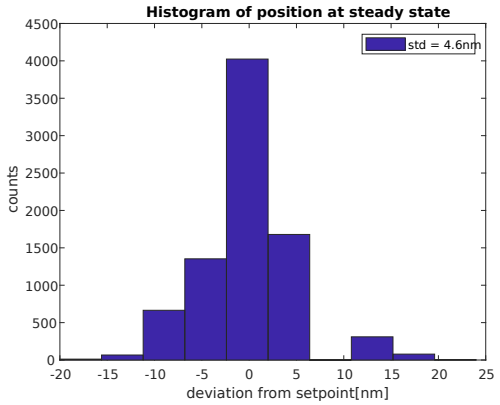

Figure 28: Position control of stage was turned off to determine the sensor noise.

3.4.6 Settling Time

The required settling time was estimated by commanding step changes and capturing the position over time. Single steps from 50 nm to 20 µm in size were recorded to obtain the settling time as function of the step size Δx. As we are dealing with a constant acceleration movement type system [42], one would expect $t_s \propto \sqrt{\Delta x}$. Fig. 29(a) shows the step response as position error over time for all the steps. The error signal has been smoothed with a uniform sliding average filter with a width of 20 samples. Fig. 29(b) shows the settling time, estimated as the time from the commanded step change until the error signal crosses 0, along with a linear fit to the data.

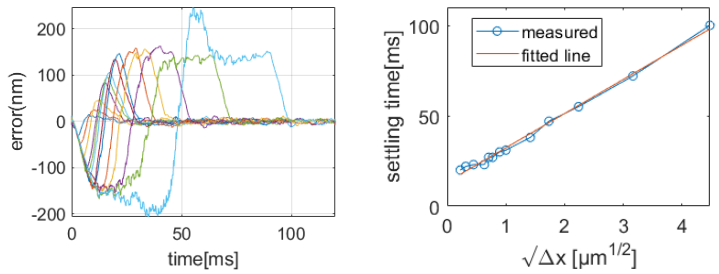

(a) (b)

Figure 29: (a) Position error of PI stage for different step sizes over time. Error signal has been smoothed with a sliding average filter with a width of 20 samples. (b) Settling time as function of the square root of step size, with fit demonstrating linear proportionality between the axes.

From the matching linear fit in Fig. 29(b), the settling time can be reasonably estimated as

$$t_s(\Delta x) = 19\sqrt{(\Delta x)} + 13.5) \tag{15}$$

where t_s is settling time in ms and Δx is the step size in µm.

As the stage response was observed to be dependent on the position and direction of travel, looking at a single step response will not give a complete picture of the stage performance. To get a better idea of the performance and to capture worst case behaviour, the response was recorded for 1000 100 nm steps at different positions and in different directions with an acquisition rate of 1 kHz. Fig. 30 shows 10 of the steps in both directions.

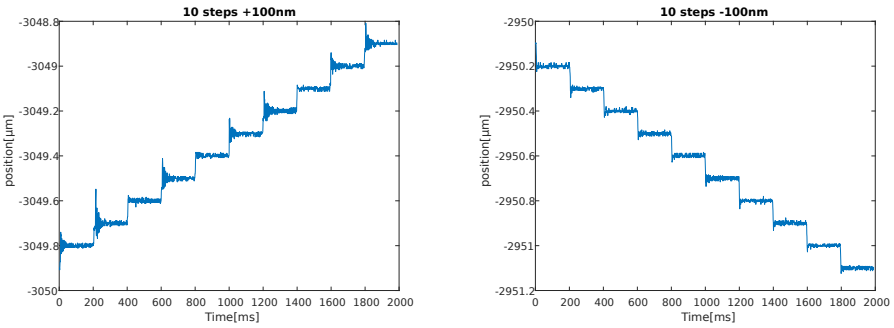

(a) 10 steps of 100 nm each in positive direction

(b) 10 steps of 100 nm each in negative direction

Figure 30: Step response of PI stage shows direction dependent asymmetry.

It is evident from the plots that the response looks different depending on the direction of travel. To estimate the settling time, the standard deviation of the commanded position over the 1000 steps is plotted for both directions in Fig. 31.

Together with the displayed maximal deviation, the non-uniformity between the two scan directions points towards a still not fully controlled oscillatory response. It can be seen that the stage is settled after approximately 40 ms when moving in the negative direction for 100 nm steps. This is about twice as long as the previously estimated value using single steps. In the case of movement in the positive direction it is apparent that there are spurious movements with large amplitude (larger than the step size itself) occurring past 100 ms, however not more than a few for the 1000 recorded steps. Nonetheless, it shows that moving in the negative direction is preferable. In the case of the negative movement direction steps, the oscillatory response has an amplitude of around 5 nm after 15 ms, which means that the waiting time may be shortened considerably if a small deviation is acceptable. Finally, the standard and maximum deviation after settling is at about 6 nm and 20 nm respectively, slightly higher than the position sensors noise.

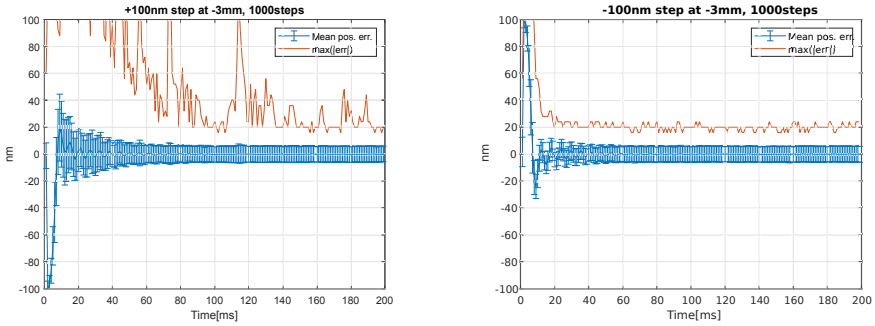

(a) 100nm steps in positive direction

(b) 100nm steps in negative direction

Figure 31: Averaged step response of Fig. 30 to determine stage settling time shows oscillatory response which is stronger in the positive direction.

3.4.7 Conclusion

The parameters of the PI-stage controller have been tuned such that the response of the stage is stable. The stage has then been characterized, showing that the position sensors can be expected to be accurate by a standard deviation of ca. 5 nm. The settling time is shown to be proportional to the square root of the step size, with the presence of an oscillatory response varying with the direction of movement. For a 100 nm step size in one direction, a completely settled response was achieved after about 40 ms, with 95% of the step size being performed after ca. 15 ms . The opposite movement showed a significantly worse response, indicating that a scan towards a specific direction is preferable when the response time is critical.

3.5 PI Stage and Camera Synchronization

3.5.1 Motivation

Having now full control of the coupling beam at the waveguide input, the last link towards efficient usage of the waveguide's multimode behaviour is the synchronization of the scanning stage with the collection optics. The according control software allows for the implementation of MUSICAL-on-chip. Following criteria should be considered for the stage to camera synchronization:

- It should be able to move the stage to a series of defined feed points, and be able to wait for the stage to reach its position.
- It should then be able to start an exposure in the camera immediately after the stage has settled.
- It should minimize the time spent doing other tasks

This section presents the software developed in Labview, displaying characteristics of the synchronized processes. Afterwards, multimode interference of a waveguide is modulated and discussed. Lastly, bioimaging is performed by

means of the synchronization software, and diffraction-limited chip imaging is compared to first MUSICAL-on-chip results.

3.5.2 Methodology

The developed software consists of three asynchronous loops communicating through a queued message system. One task handles the user interface (UI) and sends messages to the other tasks when action is required. The other two tasks are finite state machines. One takes care of handling the stage and the other the camera, each performing the actions requested by the UI-handler when commands are received through the message queue. The UI-handler has access to parameters of the stage and camera through shared variables. To avoid race-conditions, these are only read by the UI-handler. Any desired change is handled by sending appropriate commands through the message queue.

The UI-handler is an event based system. When a UI-element (buttons, sliders etc.) is changed by the user, an event is generated and a function associated with this event is called. Here, the appropriate messages are sent to the camera- and stage-handlers based on the action taken by the user, and the user interface is updated as required. Periodic tasks, such as updating the image from the microscope camera, is performed when a timer overflows. The process is illustrated in Fig. 32.

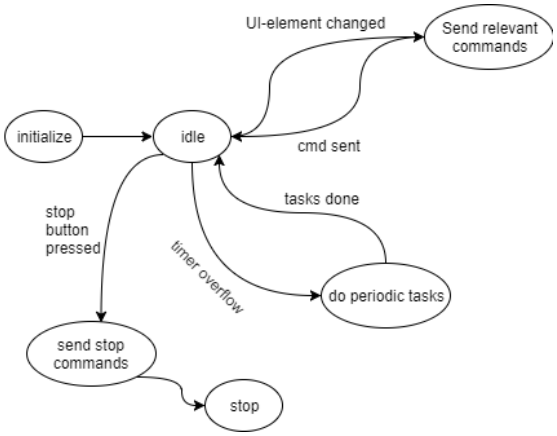

Figure 32: UI-handler of the synchronization software.

The user interface is shown in Fig. 33. Images from the camera are captured and displayed if the "Live Image"- button is enabled. The PI-stage position can be change with the slider on the left hand side. The "Get Speckle stack"-button will acquire a stack of images while shifting the feed point according to the settings in the Stage tab, saving the images to the location set in the appropriate fields. Relevant camera settings, exposure time and ROI can be set by selecting the camera tab and modifying the fields as needed. The software is available in a github repository [45].

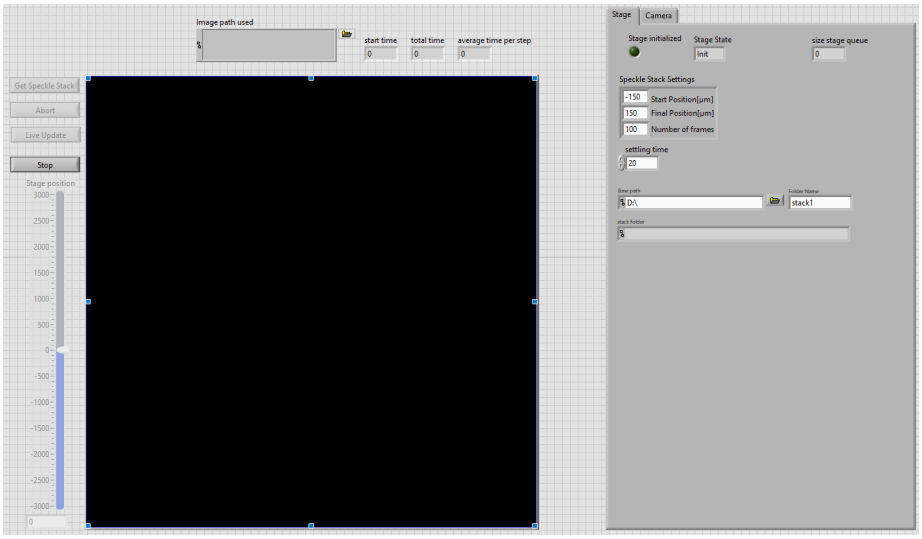

Figure 33: user interface of synchronization software.

3.5.3 Software Performance

Fig. 34(a) shows how the software divides its time for the first few frames of a stack with stage settling time and exposure time set to 20 ms. Fig. 34 (b)-(d) display histograms for each task. It can be seen how the stage task seems to spend less time than the settling time. This is likely caused by details of the method used to record the task times, and indicates a slight underestimation of the time spent here. In any case, it shows that the time spent in this task is close to ideal in most cases, though taking significantly longer (50-60 ms) for a few cases. The cause of this has not been investigated further. It could be due to USB latency or general operating system processes, although this is speculative. The camera task takes about 35 ms in most cases, rather than the ideal 20 ms. This is probably because of the image transfer from camera to computer being performed before the task is exited. The utilized Hamamatsu Orcaflash camera has a maximum transfer rate of 100 frames per second accounting for 10 ms of the camera task duration. Finally, the file task spends on average 25 ms. This is longer than the stage settling time for this example. Therefore, even though the file writing task runs concurrently with the stage task, the performance is limited as the current architecture does not allow a new exposure to be started before the file writing task has been completed. For the entire stack of 100 frames the acquisition time ends up being 6.8 seconds, while the ideal case would be 4 seconds.

3.5.4 Multimode Control

To demonstrate that the system works as intended, a 200 µm wide silicon nitride waveguide was imaged by the developed software. A stack of 2300 frames was captured using a step size of 100 nm, with the signal stemming from the waveg-

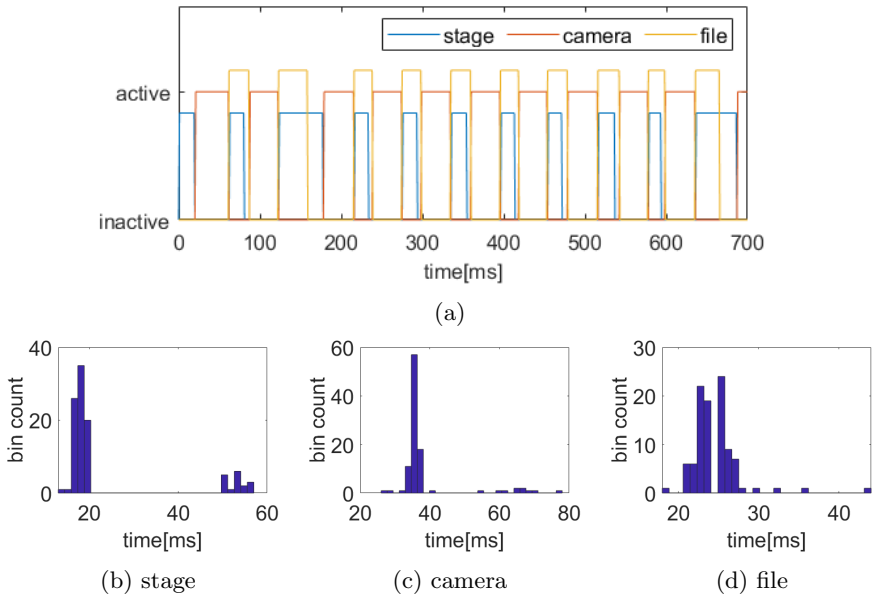

(a)

(b) stage (c) camera (d) file

Figure 34: (a) Timing diagram of the three software tasks during stage-camera synchronization, settling and exposure time being 20 ms. (b)-(d): Histograms of each task. From (b) it seems the stage task takes less than 20 ms in many cases. As the settling is implemented as a fixed delay after initiating movement of the stage, this is not possible and indicates an underestimation of the time spent here. (c) shows the camera task requiring approximately 15 ms longer than the exposure time. (d) shows that the time spent writing files is usually longer than that of the stage task, lowering performance of the system.

uide's autofluorescence excited at 561 nm (Toptica laser) and imaged through a 60x, 1.2 NA water immersion objective (Olympus) passing a long pass filter opening at 561 nm (AHF). In Fig. 35(a), a single frame from the stack is shown where an MMI-pattern is visible. Fig. 35(b) shows the mean image of the stack where an even illumination pattern is visible. The homogeneous pattern evidences that it is possible to illuminate all points of a sample on the waveguide. Fig. 35(c)-(d) show respectively a vertical and horizontal line of 35(a) whereas one axis represents the frame number the line was taken from, and therefore also the position of the feed point used to create that illumination pattern. This provides a visual indication of how the MMI-pattern in the waveguide shifts as the illumination feed point is shifted across the input facet.

3.5.5 MUSICAL-on-chip

For a bioimaging experiment, fibroblast cells from mice were isolated and seeded on a chip with 150 µm Si_3N_4 strip waveguide structures. After fixation, the sample was stained with Alexa 647 Phalloidin dye for actin imaging. Fluorescence image was excited at 660 nm (Cobolt laser) and collected by a 60x 1.2 NA water immersion objective (Olympus) passing through a long pass filter opening at

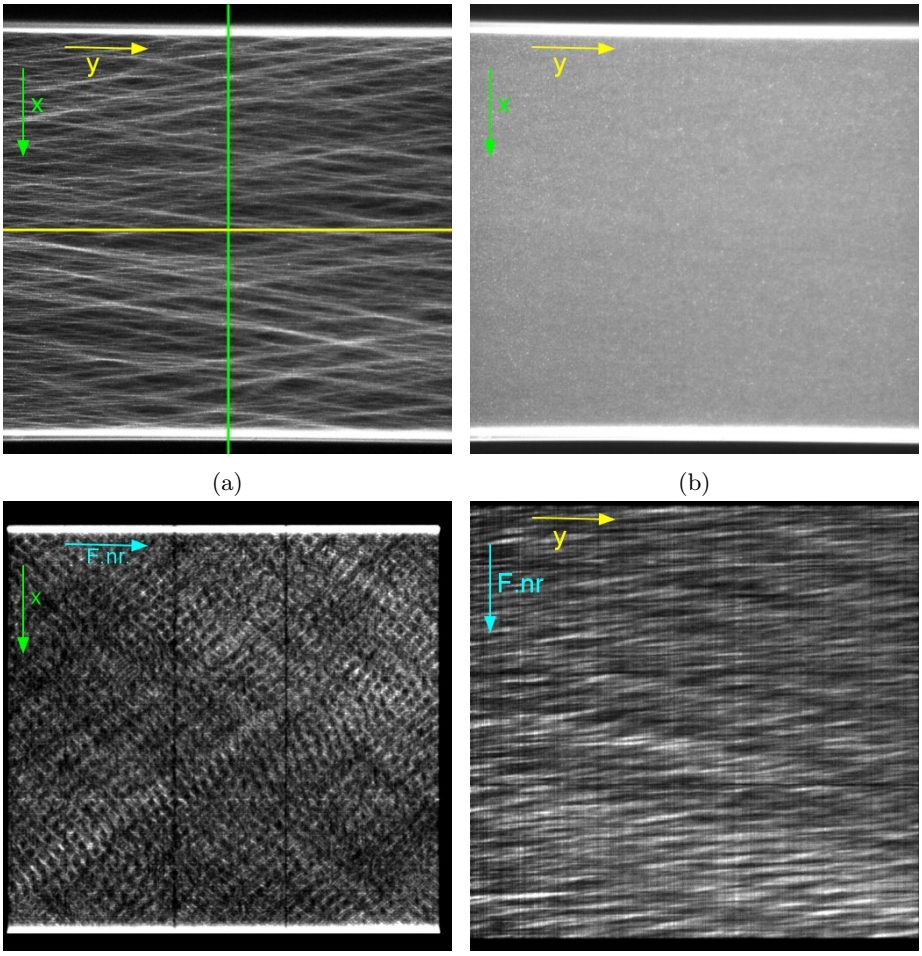

Figure 35: Illumination patterns created by scanning coupling feed point along input facet of waveguide. Waveguide width: 200 µm, 60x 1.2 NA objective, 100 nm step acquisition, 561 nm excitation, autofluorescence signal. (a) Single frame of the stack, with visible interference patterns. Green and yellow lines indicate the pixels used to create (c) and (d), respectively. (b) Mean image of the stack, demonstrating complete illumination of waveguide surface. In (c) and (d), one axis corresponds to the line from (a) scanned over the stack, respective axes indicated in each image. This illustrates the light modulation over each axis.

664 nm and a notch filter enabling transmission at 692 ± 40 nm (both from AHF). A 100 nm step size coupling scan of 281 frames was performed on a 320 µm wide waveguide, with results presented in Fig. 36. In Fig. 36(a), a single frame of the stack is shown, with inhomogeneous intensity due to mode interference. In Fig. 36(b), an average of the stack successfully removes the fluctuations seen in (a). Fig. 36(c) presents the MUSICAL rendering of the data. The MUSICAL results are compared to the mean image in (d). It can be seen how the actin lines are better resolved by MUSICAL on denser regions. White lines on the two images indicate the region of a line profile plotted in (e). Whereas the plotted region could not be resolved by the mean image, the MUSICAL results point towards three actin lines in that region. Considering the wavelength and the utilized numerical aperture of the objective, the theoretical resolution for an optimized diffraction-limited system would be ca. 280 nm, Aberrations in the collection system are thus very evident. Nevertheless, the full width at half maximum of the central peak resolved using MUSICAL is ca. 150 nm, showing an over two-fold resolution improvement over the ideal theoretical value for first, not optimized MUSICAL-on-chip results.

3.5.6 Conclusion

The synchronization between coupling stage and camera was developed in a Labview interface and characterized for its performance. Comparing the time spent at each task it was shown that the program runs efficiently but not at ideal speed, which could possibly be implemented through a different program architecture. The program was used for a homogeneous signal at the waveguide surface (autofluorescence), demonstrating that mode scanning can illuminate the entirety of the surface. Finally, a first bioimaging experiment demonstrated MUSICAL-on-chip, considerably enhancing the resolution of a sample.

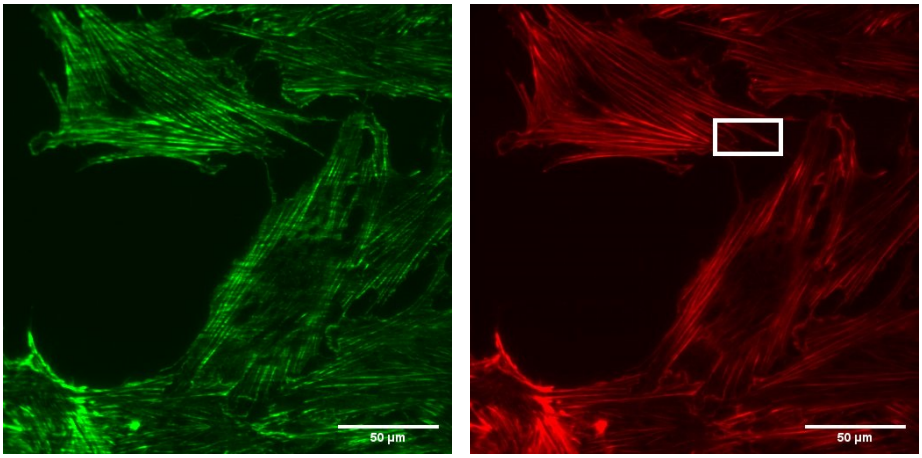

(a) Single frame (b) Mean image

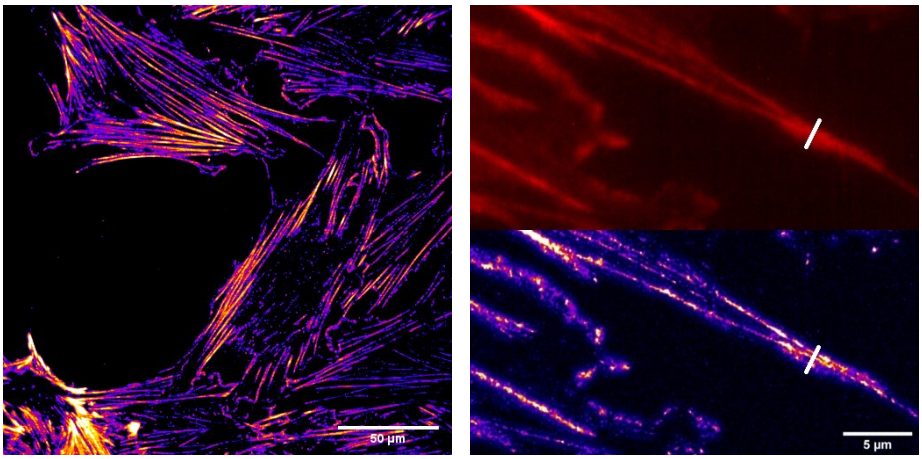

(c) MUSICAL image (d) Mean(top) and MUSICAL(bottom)

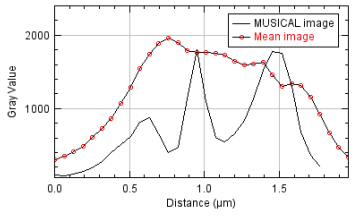

(e) Line profiles indicated in (d)

Figure 36: Fibroblast cells from mice imaged for actin on the chip setup. A stack of 281 images with 100 nm step size of the illumination spot was taken from a 320 µm wide, 150 nm tall Si_3N_4 strip waveguide. (a) Single frame of stack, showing multimode interference. (b) Mean image, removing multimode interference. (c) MUSICAL rendering of data. (d) Comparison between mean and MUSICAL images, with indicated line profile plotted in (e). The large improvement in resolution through the MUSICAL algorithm is visible at the dense signal region.

4 Discussion and Outlook

4.1 Summary of the accomplished work

The purpose of this master's thesis was to take steps towards making chip based nanoscopy more practical and user friendly. These two points were identified as the biggest issues and therefore the scope of the thesis:

- Lack of an easy, fast, and reliable method of coupling light into waveguides
- Lack of suitable automatic system for the control and synchronization of camera and illumination modulation system such that MUSICAL-on-chip can be realized.

While a novel illumination set-up, more amenable to optimization for automatic coupling, was designed by Azeem Ahmed, design of the process of automatic coupling was achieved as a part of this thesis. A novel edge finding algorithm based on analysis of the shape of the excitation beam was made. Using this algorithm allowed characterization of the coupling stage's inter-axis crosstalk. This significantly reduced the difficulty of achieving initial coupling by allowing correction of the axis crosstalk from over 70 μm to less than 3 and 1 μm for the $y-$ and $z-$axes respectively. Further, two different optimization algorithms, namely Gradient Descent and the Nelder-Mead simplex method, are explored as candidates for automatically optimizing the coupling efficiency after the initial coupling has been done. This is done by modelling the coupling efficiency as a function of misalignment of the excitation light beam with a waveguides input facet. The Nelder-Mead simplex optimization algorithm exhibited superior performance in terms of speed and noise immunity, hence was selected to be implemented on the setup. Testing of the method as implemented showed promising results with close to optimal coupling efficiency achieved in a reasonable amount of time.

The second issue was further divided into two tasks:

- Controlling the multimode illumination patterns that can be induced in the waveguide by precisely controlling the feed point location, its stability, and stepping across the width of the waveguide
- Developing a synchronized work flow for synchronizing the illumination mode control with the camera's image acquisition and writing of image data into the memory, being able to repeat this work flow continuously and automatically for acquiring several thousand images (if needed), and making a simple user interface for using the system.

Images acquired under the different illumination patterns are needed for realizing MUSICAL-on-chip. Varying the feed point of the illumination across the input facet of the multimode waveguide modulates the illumination patterns in it. This is accomplished by a piezoelectric stage with large travel range. The piezoelectric stage was completely characterized for resolution, stability, settling time, etc. and then tuned for optimal performance in terms of speed and accuracy. The performance of the tuned piezoelectric stage was then characterized, providing the information needed to implement synchronized workflow.

Synchronization and automatic execution of the workflow of the various components of photonic-chip based microscope, including the automatic coupling, piezeoelectric stage for multimode illumination control, camera acquisition, writing of data file into the computer and repeating the process in a controlled manner over specified range was accomplished through Labview. Beside designing a workflow, the work needed characterization of the time taken by each task in the work flow as well as exception handling. A user interface was also designed for the purpose.

The aspects that could have been interesting to consider are briefly discussed below:

- A more extensive study of variety of algorithms and objetcive functions for automatic coupling could have been conducted.
- A more extensive characterization of the coupling efficiency as a function of all degrees of freedom of the input coupling set-up could have been undertaken. Its repeatability over multiple independent experiments and its variation over the wavelength and the type of illumination could have been undertaken.
- The automatic and synchronous work flow could have been subjected to exhaustive exception handling. A better and more user-friendly interface could have been designed.

These aspects were not undertaken because of either or both of the following reasons. First, the time or experimental conditions needed for them could be impractically demanding. Second, in the current state of the technology, these aspects would provide minor incremental benefit over the work already accomplished in this thesis.

4.2 Impact of the Accomplished Work

Now, the impact of the work undertaken in this thesis is presented in terms of the three main contributions.

Automatic coupling: There are two aspects of the impact of automatic coupling, namely the achieved coupling efficiency and the time taken for the coupling efficiency. In the example shown in Fig. 24, the coupled light increased from 3 μW at initial coupling to 21 μW after automatic coupling, and that too within 11 seconds only. In comparison, a trained and experienced person may achieve similar coupling efficiency, but typically needs 3-5 minutes for achieving that. There is no good way to characterize the reduction in photo-damage of the sample due to the reduction in the time needed for coupling, but it is obvious that reduction of the time by approximately 10 times implies a significant advantage in terms of reduced photo-damage. Moreover, since the manual coupling is mostly heuristic, the assurance of good coupling efficiency is weak and the manual optimization is terminated as soon as a heuristically reasonable signal is seen in the camera. This often means that manual coupling may often lead to less than optimal coupling efficiency and consequently less than optimal signal to noise ratio. Since the signal to noise ratio is a critical

factor in determining the achievable resolution in nanoscopy [31], the impact of near-optimal and systematically achieved coupling efficiency on the microscopy and nanoscopy system performance is immense.

Controlled multimode illumination: MUSICAL-on-chip benefits from illumination pattern variation. However, for this several images have to be taken with the different positions of the feed point. Practically, the number of electromagnetic modes that can be induced in the waveguide and therefore the degree of variation in the illumination pattern of the waveguide is limited. In an ongoing work, it was deemed important to derive maximum available illumination variation with minimum number of measurements in order to enable fast nanoscopy as well as minimize the photo-damage to the sample. For this, systematic analysis of illumination pattern was necessary, and as an implication, the ability to acquire illumination patterns in a controlled manner was essential. This was made possible using the controlled multimode illumination accomplished in this thesis. Although the outcome of this work is not yet published, the work accomplished paved the path for not only identifying the sufficient distance between consecutive feed points for a given waveguide geometry and wavelength, it also assured that imaging the sample with this sufficient distance is possible in a stable manner.

Automatic and synchronous work flow: Previously, even for nanoscopy, the feed point was continuously scanned and camera would independently acquire images of the sample even as the illumination patterns varied continuously even within a single acquisition. Since MUSICAL-on-chip intends to exploit the high spatial frequency of the illumination pattern, the previous acquisition was specifically unsuitable. This is because the average illumination over a single image acquisition worked as low pass filter, removing some amount of high spatial frequency content. This meant that MUSICAL-on-chip needed one image per position of the feed point. A manual acquisition for a few hundred images would mean about 10 second per image for switching the position, beginning the image acquisition, and closing the camera before switching to the next position. For a few hundred images, it would mean several to a few hours of imaging, even if the exposure time is in the order of milliseconds per image. The sample would continuously remain exposed to the light and experience photo-damage to the extent that it would completely bleach out. Therefore, MUSICAL-on-chip was practically not achievable before this thesis. The automatic work flow ensures that the fallow time between two consecutive is as low as possible while providing sufficient stability of illumination. Therefore, the imaging of few hundred images is now in the order of seconds and MUSICAL-on-chip is made feasible, as demonstrated in the results in chapter 3.

4.3 Future Outlook

The photonic-chip based microscopy and nanoscopy technology has a huge research and commercial potential. In the future, development on the following aspects, from the perspective of instrumentation and automation, will be beneficial:

- Supporting electronic or automatic switching between different imaging

modalities, for example, TIRF microscopy, MUSICAL-on-chip, ESI, and single molecule localization, will be useful. Furthermore, automatic execution of the relevant reconstruction algorithm in the background can be beneficial.

- Integration and automatic one-click execution of all the steps from the moment the chip is placed on the sample to the moment that the user selects the imaging modality will dramatically improve the usability of photonic-chip illumination, and even contribute to improving its technology readiness.
- Automatic determination and recommendation of the experimental parameters, such as distance between the feed points, exposure time of the camera, etc. can be useful.
- Efforts towards making MUSICAL-on-chip as an algorithm executed immediately after the camera in real time can greatly reduce the image storage needs and processing time needed for performing photonic-chip nanoscopy.

References

[1] Abbe. The relation of aperture and power in the microscope. *Journal of the Royal Microscopical Society*, 2(3):300–309, June 1882.

[2] E. Abbe. VII.-on the estimation of aperture in the microscope. *Journal of the Royal Microscopical Society*, 1(3):388–423, June 1881.

[3] S.W. Hell, S.J. Sahl, M. Bates, X. Zhuang, R. Heintzmann, M.J. Booth, J. Bewersdorf, G. Shtengel, H. Hess, P. Tinnefeld, A. Honigmann, S. Jakobs, I. Testa, L. Cognet, B. Lounis, H. Ewers, S.J. Davis, C. Eggeling, D. Klenerman, K.I. Willig, G. Vicidomini, M. Castello, A. Diaspro, and T. Cordes. The 2015 super-resolution microscopy roadmap. *Journal of Physics D: Applied Physics*, 48(44), 2015.

[4] Robin Diekmann, Øystein I. Helle, Cristina I. Øie, Peter McCourt, Thomas R Huser, Mark Schüttpelz, and Balpreet S. Ahluwalia. Chip-based wide field-of-view nanoscopy. *Nature Photonics*, 11(5):322–328, 5 2017.

[5] Jean-Claude Tinguely, Øystein Ivar Helle, and Balpreet Singh Ahluwalia. Silicon nitride waveguide platform for fluorescence microscopy of living cells. *Opt. Express*, 25(22):27678–27690, Oct 2017.

[6] S. Andre Solbø O. G. Hellesø F. Tsige Dullo, J. Tinguely. Single-mode limit and bending losses for shallow rib si3n4 waveguides. *IEEE Photonics Journal*, 7(1):1–11, Feb 2015.

[7] Øystein I. Helle, David A. Coucheron, Jean-Claude Tinguely, Cristina I. Øie, and Balpreet S. Ahluwalia. Nanoscopy on-a-chip: super-resolution imaging on the millimeter scale. *Opt. Express*, 27(5):6700–6710, Mar 2019.

[8] Krishna Agarwal and Radek Machán. Multiple signal classification algorithm for super-resolution fluorescence microscopy. *Nature Communications*, 7:13752 EP –, Dec 2016. Article.

[9] Wikipedia. Snell's law — Wikipedia, the free encyclopedia. `http://en.wikipedia.org/w/index.php?title=Snell's%20law&oldid=895834446`, 2019. [Online; accessed 12-May-2019].

[10] Jin Au Kong. *Theory of electromagnetic waves*. Wiley New York, 1975.

[11] Wikipedia. Evanescent field — Wikipedia, the free encyclopedia. `http://en.wikipedia.org/w/index.php?title=Evanescent%20field&oldid=894791067`, 2019. [Online; accessed 14-May-2019].

[12] Ginés Lifante. *Integrated Photonics: Fundamentals*, pages 58–60. John Wiley & Sons, Ltd, January 2003.

[13] Photon Design. `https://www.photond.com/products/fimmprop/fimmprop_applications_03.htm`[Accessed: 30.04.19].

[14] Shankar Kumar Selvaraja and Purnima Sethi. *Review on Optical Waveguides*. InTech, 08 2018.

[15] Ulrike Endesfelder and Mike Heilemann. *Direct Stochastic Optical Reconstruction Microscopy (dSTORM)*, pages 263–276. Springer New York, New York, NY, 2015.

[16] `https://www.wur.nl/en/show/Superresolution-Microscopy.htm`. [online; accessed 11-may-2019].

[17] H.M. Grandin, B. Städler, M. Textor, and J. Vörös. Waveguide excitation fluorescence microscopy: A new tool for sensing and imaging the biointerface. *Biosensors and Bioelectronics*, 21(8):1476 – 1482, 2006.

[18] Björn Agnarsson, Saevar Ingthorsson, Thorarinn Gudjonsson, and Kristjan Leosson. Evanescent-wave fluorescence microscopy using symmetric planar waveguides. *Optics express*, 17:5075–82, 04 2009.

[19] Björn Agnarsson, Asta B. Jonsdottir, Nina B. Arnfinnsdottir, and Kristjan Leosson. On-chip modulation of evanescent illumination and live-cell imaging with polymer waveguides. *Opt. Express*, 19(23):22929–22935, Nov 2011.

[20] Hao Shen, Eric Huang, Tapaswini Das, Hongxing Xu, Mark Ellisman, and Zhaowei Liu. Tirf microscopy with ultra-short penetration depth. *Opt. Express*, 22(9):10728–10734, May 2014.

[21] Srinivasan Ramachandran, Daniel A Cohen, Arjan Quist, and Ratnesh Lal. High performance, led powered, waveguide based total internal reflection microscopy. *Scientific reports*, 3:2133, 07 2013.

[22] Björn Agnarsson, Anders Lundgren, Anders Gunnarsson, Michael Rabe, Angelika Kunze, Mokhtar Mapar, Lisa Simonsson, Marta Bally, Vladimir P. Zhdanov, and Fredrik Höök. Evanescent light-scattering microscopy for label-free interfacial imaging: From single sub-100 nm vesicles to live cells. *ACS Nano*, 9(12):11849–11862, 2015. PMID: 26517791.

[23] David A. Coucheron, Øystein I. Helle, Christina I. Øie, Firehun Tsige Dullo, and Balpreet S. Ahluwalia. Chip-based nanoscopy: towards integration and high-throughput imaging. In Prabhat Verma and Alexander Egner, editors, *Nanoimaging and Nanospectroscopy V*, volume 10350. SPIE, December 2017.

[24] Mike Heilemann, Sebastian van de Linde, Mark Schüttpelz, Robert Kasper, Britta Seefeldt, Anindita Mukherjee, Philip Tinnefeld, and Markus Sauer. Subdiffraction-resolution fluorescence imaging with conventional fluorescent probes. *Angewandte Chemie International Edition*, 47(33):6172–6176, August 2008.

[25] M. G. L. Gustafsson. Surpassing the lateral resolution limit by a factor of two using structured illumination microscopy. COMMUNICATION. *Journal of Microscopy*, 198(2):82–87, May 2000.

[26] I. Yahiatene, S. Hennig, M. Müller, and T. Huser. Entropy-based superresolution imaging (esi): From disorder to fine detail. *ACS Photonics*, 2(8):1049–1056, 2015.

[27] Nils Gustafsson, Siân Culley, George Ashdown, Dylan M. Owen, Pedro Matos Pereira, and Ricardo Henriques. Fast live-cell conventional fluorophore nanoscopy with ImageJ through super-resolution radial fluctuations. *Nature Communications*, 7(1), August 2016.

[28] T. Dertinger, R. Colyer, G. Iyer, S. Weiss, and J. Enderlein. Fast, background-free, 3d super-resolution optical fluctuation imaging (SOFI). *Proceedings of the National Academy of Sciences*, 106(52):22287–22292, December 2009.

[29] Graham T Dempsey, Joshua C Vaughan, Kok Hao Chen, Mark Bates, and Xiaowei Zhuang. Evaluation of fluorophores for optimal performance in localization-based super-resolution imaging. In *Nature Methods*, 2011.

[30] MinKwan Kim, Chung-Hyun Park, Yong-Hoon Cho, and YongKeun Park. Super resolution microscopy with induced optical fluctuation. *Biophysical Journal*, 110:175a, 02 2016.

[31] Krishna Agarwal and Dilip K. Prasad. Eigen-analysis reveals components supporting super-resolution imaging of blinking fluorophores. *Scientific Reports*, 7(1):4445, 2017.

[32] Texas Instruments. Opa2336 single-supply, micropower cmos operational amplifiers microamplifier series. `http://www.ti.com/product/OPA2336`. [Online; accessed 10-May-2019].

[33] Adafruit. adafruit/adafruit_ads1x15. `https://github.com/adafruit/Adafruit_ADS1X15`. [Online; accessed 09-May-2019].

[34] Daniel Henry Hansen. Photodiode acquisition board. `https://github.com/dha010/Photodiode-acquisition-board`, May 2019.

[35] Thorlabs. Max300 series nanomax 3-axis flexure stage user guide. `https://www.thorlabs.com/thorproduct.cfm?partnumber=MAX381/M`. [Online; accessed 13-May-2019].

[36] Daniel Henry Hansen. coupling optimization and edgefinding algorithm implemented in labview. `https://github.com/dha010/Optimization`, May 2019.

[37] Wikipedia. Gradient descent — Wikipedia, the free encyclopedia. `http://en.wikipedia.org/w/index.php?title=Gradient%20descent&oldid=896643399`, 2019. [Online; accessed 13-May-2019].

[38] Jonathan Barzilai and Jonathan M. Borwein. Two-point step size gradient methods. *IMA Journal of Numerical Analysis*, 8(1):141–148, 1988.

[39] Nelder–Mead method. Nelder–mead method — Wikipedia, the free encyclopedia. [Online; accessed 30.04.19].

[40] S. Singer and J. Nelder. Nelder-Mead algorithm. *Scholarpedia*, 4(7):2928, 2009. revision #91557.

[41] Margaret L. Tuma and Glenn Beheim. Calculated coupling efficiency between an elliptical-core optical fiber and a silicon oxynitride rib waveguide. *NASA Tech. Memo. 106850*, 02 1995.

[42] Mark Frier. Reliability of q-motion® systems. `https://www.physikinstrumente.com/en/technology/piezoelectric-drives/piezo-inertia-drives`. Version: WP4009.

[43] PI. Pz241e e-871 pishift controller user manual. Available from Physik Instrumente on request.

[44] Wikipedia. PID controller — Wikipedia, the free encyclopedia. `http://en.wikipedia.org/w/index.php?title=PID%20controller&oldid=895176774`, 2019. [Online; accessed 09-May-2019].

[45] Daniel Henry Hansen. Chip-based-microsope-control. `https://github.com/dha010/Chip-Based-Microsope-control`, May 2019.